ACDL/DQ-1 Calibration Algorithms. Part I: Nighttime 532 nm Polarization and High-Spectral-Resolution Channel

Fanqian Meng[1], Junwu Tang[2], Guangyao Dai[1], Wenrui Long[1], Kangwen Sun[1], Zhiyu Zhang[1], Xiaoquan Song[1,2], Jiqiao Liu[3], Weibiao Chen[3], Songhua Wu[1,2,4]

5 [1]College of Marine Technology, Faculty of Information Science and Engineering, Ocean University of China, Qingdao, 266100, China
[2]Laoshan Laboratory, Qingdao, 266200, China
[3]Key Laboratory of Space Laser Communication and Detection Technology, Shanghai Institute of Optics and Fine Mechanics, Chinese Academy of Sciences, Shanghai 201800, China
10 [4]Institute for Advanced Ocean Study, Ocean University of China, Qingdao, 266100, China

Correspondence to: Guangyao Dai, daiguangyao@ouc.edu.cn

Abstract. The Atmospheric Environment Monitoring Satellite (DQ-1) was successfully launched in April 2022, with the capability of providing continuous multi-sensor spatial and optical simultaneous observations of carbon dioxide, aerosols and

15 clouds. The primary payload carried on DQ-1 is an Aerosol and Carbon dioxide Detection Lidar (ACDL). The instrument comprises a high-spectral-resolution channel at 532 nm, polarization channels at 532 nm, elastic scattering channel at 1064 nm, and integrated-path differential absorption (IPDA) channel at 1572 nm. The optical properties of aerosols and clouds measured by the ACDL promote a quantitative characterization of the uncertainties in the global climate system, hence the precise calibrations for the ACDL are necessary. This paper outlines the algorithms employed for calibrating the nighttime

20 532 nm measurements for the first spaceborne high-spectral-resolution lidar with an iodine vapor absorption filter. The nighttime calibrations of the 532 nm data are fundamental to the ACDL measurement procedure, as they are utilized to derive the calibrations over daytime orbits and the calibrations of the 1064 nm channel relative to the 532 nm channel. This paper provides a review of the theoretical foundations for molecular normalization techniques as applied to spaceborne lidar measurements, includes a detailed discussion of auxiliary data and theoretical parameters used in ACDL calibrations, as well

25 as a comprehensive description of the calibration algorithm procedure. To mitigate large errors stemming from high-energy events during calibration, a data filter is designed to obtain valid calibration signals. The paper also assesses the results of the calibration procedure, by analyzing the errors of calibration coefficients and validating the attenuated backscatter coefficient results. The results indicate that the relative error of the calibrated attenuated backscatter coefficients is lower than 1% in the calibration area, and the uncertainty of the clear-air scattering ratio was within anticipated range of 6%.

1 Introduction

The Atmospheric Environment Monitoring Satellite (DQ-1), which was launched on April 16, 2022, is a research satellite designed to monitor the atmospheric environment. It is equipped with five payloads (Zhu et al., 2023) including an Aerosol and Carbon dioxide Detection Lidar (ACDL), a Particulate Observing Scanning Polarimeter (POSP), a Directional Polarization Camera (DPC), an Environmental Trace Gases Monitoring Instrument (EMI), and a Wide Swath Imager (WSI). The primary payload is the ACDL, which is a lidar system consisting of two different modules. One is the aerosol-measurement module which measures profiles of clouds and aerosols with high accuracy globally, and another is the CO_2 measurement module for atmospheric column CO_2 observations (Liu et al., 2019; Wang et al., 2020). The scientific objective of the ACDL is to detect high-resolution vertical profiles of global atmospheric aerosols and clouds. It aims to explore the optical features of atmospheric aerosols and clouds, and gather information related to the distribution of global atmospheric column CO_2 concentrations, and provide precise quantitative scientific data for determining the sources and sinks of CO_2 (Chen et al., 2023). To enable ACDL quantitative measurement of atmospheric parameters, accurate calibration of the raw measurement data is necessary. The spaceborne lidar signal comprises lidar instrument characteristics, measured distance, particle backscatter signal and atmospheric attenuation. The calibration procedure for the spaceborne lidar is defined as the construction of a quantitative relationship between the particle (include both molecules and aerosol) backscatter signal and the corresponding lidar signal. The calibration procedure calculates the calibration coefficients for each channel and applies the calibration coefficients to the original profiles to obtain the attenuated backscatter coefficients. The nighttime 532 nm polarization and high-spectral resolution channels (hereafter referred to as HSRL channel) of the ACDL were calibrated utilizing molecular normalization calibration techniques. The calibrations are conducted in areas with a clean atmosphere, wherein the presence of aerosols and clouds is assumed to be absent, all backscattered light is generated from molecules. The accurate estimation of the expected molecular backscatter and attenuation is calculated from the European Centre for Medium-Range Weather Forecasts (ECMWF) atmospheric assimilation model of the fifth generation reanalysis (ERA5) dataset (Hersbach et al., 2020). The aerosol loading within the calibration region is evaluated by utilizing the aerosol data from Stratospheric Aerosol and Gas Experiment-III (SAGE III, Cisewski et al., 2014; Knepp et al., 2020). The resulting calibrated attenuated backscatter coefficient product serves as a foundation for the subsequent lidar products, with accurate calibration results being crucial for ensuring the credibility of those products.

The currently operational spaceborne lidars have formulated calibration algorithms based on the molecular normalization calibration technique specific to their own characteristics, and conducted calibrations in clean atmospheric regions. The Lidar In-space Technology Experiment (LITE) lidar system uses data at the height of 30 and 34 km to derive calibration coefficients for the 355 nm and 532 nm channels, with calibration coefficients maintained at a range of ±5% (Osborn, 1998; Russell et al., 1979). Based on the experiences of the LITE, the Cloud-Aerosol Lidar and Infrared Pathfinder Satellite Observations (CALIPSO) employs a calibration approach using molecular normalization technique applicable to the 532 nm, and cirrus spectral backscatter ratio for the 1064 nm channels of the Cloud-Aerosol Lidar with Orthogonal Polarization (CALIOP, one

of instruments aboard the CALIPSO). The calibration of the CALIOP underwent four versions, in the first three versions, the atmosphere was used as the calibration altitude at 30– 34 km consistent with LITE (Reagan et al., 2002; Hostettler et al., 2006;

65   Powell et al., 2009). Additionally, the CALIPSO scientific team has formulated calibration algorithms for the 532 nm daytime orbit and the 1064 nm channel (Powell et al., 2010; Vaughan et al., 2010).   However, the studies have shown that aerosols within the 30–34 km exhibit temporal and spatial variabilities, indicating that they cannot be disregarded (Vernier et al., 2009). Therefore, CALIPSO updated the stratospheric molecular normalization region up to 36–39 km in a subsequent revision and adjusted the corresponding algorithms (Kar et al., 2018). Additionally, the calibration algorithms for the 532 nm daytime and

70   1064 nm channels were also revised (Getzewich et al., 2018; Vaughan et al., 2019). The Cloud-Aerosol Transport System (CATS) that flew on the International Space Station (ISS) was designed for detecting cloud and aerosol. Since its 1064nm calibration region was selected between 23 and 27 km, it cannot fully disregard aerosol effects and the system also considers the impact of the aerosol stratospheric scattering ratio (Yorks et al., 2015; Pauly et al., 2019). Compared to cloud and aerosol detection lidars like CALIPSO, the the Ice, Cloud, and land Elevation Satellite (ICESat) series of satellites, primarily focus on

75   measuring the elevation of ice sheets, glaciers, sea ice and more. They are calibrated using molecular normalization technique as well. The calibration altitude range for the Geoscience Laser Altimeter System (GLAS) on ICESat was selected as 26–30 km (Palm et al., 2011), whereas the Advanced Topographic Laser Altimeter System (ATLAS) lidar system on its improved instrument ICESat-2 chose the region of 11–13.5 km altitude for calibration due to data frame limitations (Palm et al., 2021). Furthermore, the Atmospheric LAser Doppler INstrument (ALADIN) onboard ADM-Aeolus (Atmospheric Dynamics

80   Mission-Aeolus), was a direct detection Doppler Wind Lidar operated in the ultra-violet region, also performed the calibration of attenuated backscatter coefficient. The ALADIN sets the calibration in the atmospheric altitude range of 6–16 km at mid to high latitudes. The calibration coefficients for Rayleigh and Mie scattering channels are also calibrated using the molecular normalized technique (Pierre et al., 2020). The upcoming deployment of the ATmospheric LIDAR (Light Detection and Ranging) lidar system, ATLID, is part of the payload of Earth Cloud, Aerosol and Radiation Explorer (EarthCARE) mission

85   has nearly finished ground-based calibration and performance verifications, with post-launch on-orbit calibrations scheduled to follow (Wehr et al., 2023).
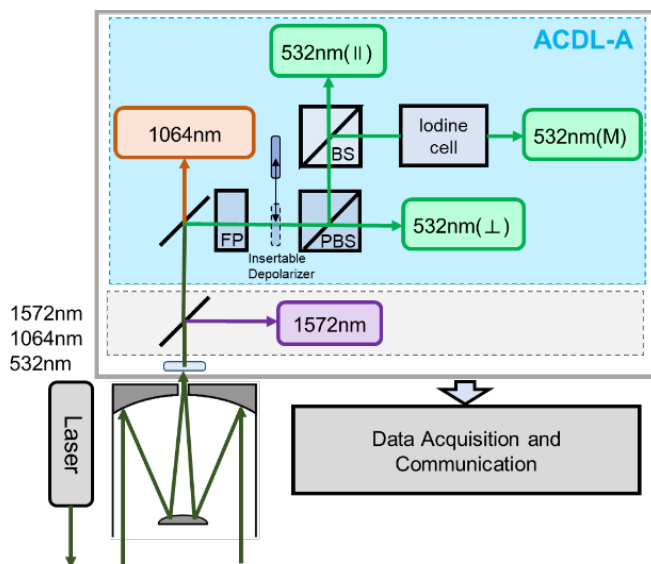
Figure 1: Schematic diagram of ACDL (duplication from Dai et al., 2024).

The ACDL receiver subsystem gathers the echoed signal through five channels: three channels at 532 nm, one channel at 1064
90   nm, and one channel at 1572 nm, as illustrated in Figure 1. After passing through the polarization beam splitter (PBS), the 532 nm signals are split into perpendicular-polarized and parallel-polarized components separately. The entire parallel-polarized signal passes through a beam splitter (BS), a portion (70%) of the signal through an iodine vapor absorption filter to block Mie scattering, thus constituting the high-spectral-resolution channel. The remaining signal enters the parallel-polarization channel. The backscattered photons then excite the photomultiplier tube (PMT) located in each channel, which converts light into
95   electrical signals. The calibration procedure converts electrical signals to backscatter coefficients for calculating atmospheric and aerosol products. The ACDL scientific team has initially achieved total depolarization ratio, backscatter coefficient, extinction coefficient, lidar ratio, color ratio, and other optical parameter products of aerosols and clouds. These products provide a characterization of the rich vertical structure of global aerosols and clouds in both vertical and horizontal directions (Dai et al., 2024).

100   This paper outlines the calibration methodology for the ACDL 532 nm parallel channel, perpendicular channel and high spectral resolution channel, shows the results of the global calibration coefficients and attenuated backscatter coefficients, and assesses the results. Section 2 describes the calibration algorithms for the ACDL. Section 3 highlights the corresponding validation methods applied. Discussions, conclusions and outlook are summarized in Sections 4 and 5.

2. Nighttime Calibration Algorithms and methodology

105   Calibration procedure is a fundamental element of processing spaceborne lidar data, and its aim is to establish a quantitative relationship between the particle backscatter coefficient and the electrical signals detected by the lidar system. The ACDL 532

nm channel comprises three channels that receive parallel-polarized signal, perpendicular-polarized signal and high-spectral-resolution signal. The maximum measurement altitude of the ACDL is defined as the "time delay", which was the time between the emission of the odd pulse and the start of signal acquisition, the maximum altitude fluctuates in the range of 36-40 km (Dai

110   et al., 2024). The calibration procedure is applied to the original background removed, range-scaled energy and gain-normalized signal. It requires system parameters, including signal distance, pulse energy, gain and so on. Among these, the output pulse energy of the ACDL laser pulse is measured by an energy monitor. Table 1 lists the lidar parameters utilized for the calibration.

Table 1: Parameters of the ACDL instrument for calibration

Parameters	Value
Wavelength	532.245 nm;
Pulse Energy	~130 mJ@532 nm;
Gain	59.46@parallel; 53.46@perpendicular; 32.00@ high-spectral-resolution
Lidar Off-Nadir Angle	2°
Laser Repetition Frequency	40Hz@532nm
Optical Filter Line Widths	<30pm
Telescope Area	1 m
Vertical Resolution	3 m@<7.5 km; 24 m (8 bin average) @>7.5 km
Horizontal Resolution	~ 330 m
Orbit Altitude	705 km
Orbit Inclination	98°
Polarization Purity for PBS	1000:1

115   Both the nighttime parallel and high-spectral-resolution channels of ACDL are calibrated using the molecular normalization calibration technique, began with the denoised original data. The minimum values of the segmented-averaged signal in the parallel-polarized channel and perpendicular-polarized channel of 532 nm are selected as background noise (Yorks et al., 2015; Pauly et al., 2019; Palm et al., 2022), while the signals at high altitude are removed as background noise in the high-spectral-resolution channel (Dai et al., 2024).
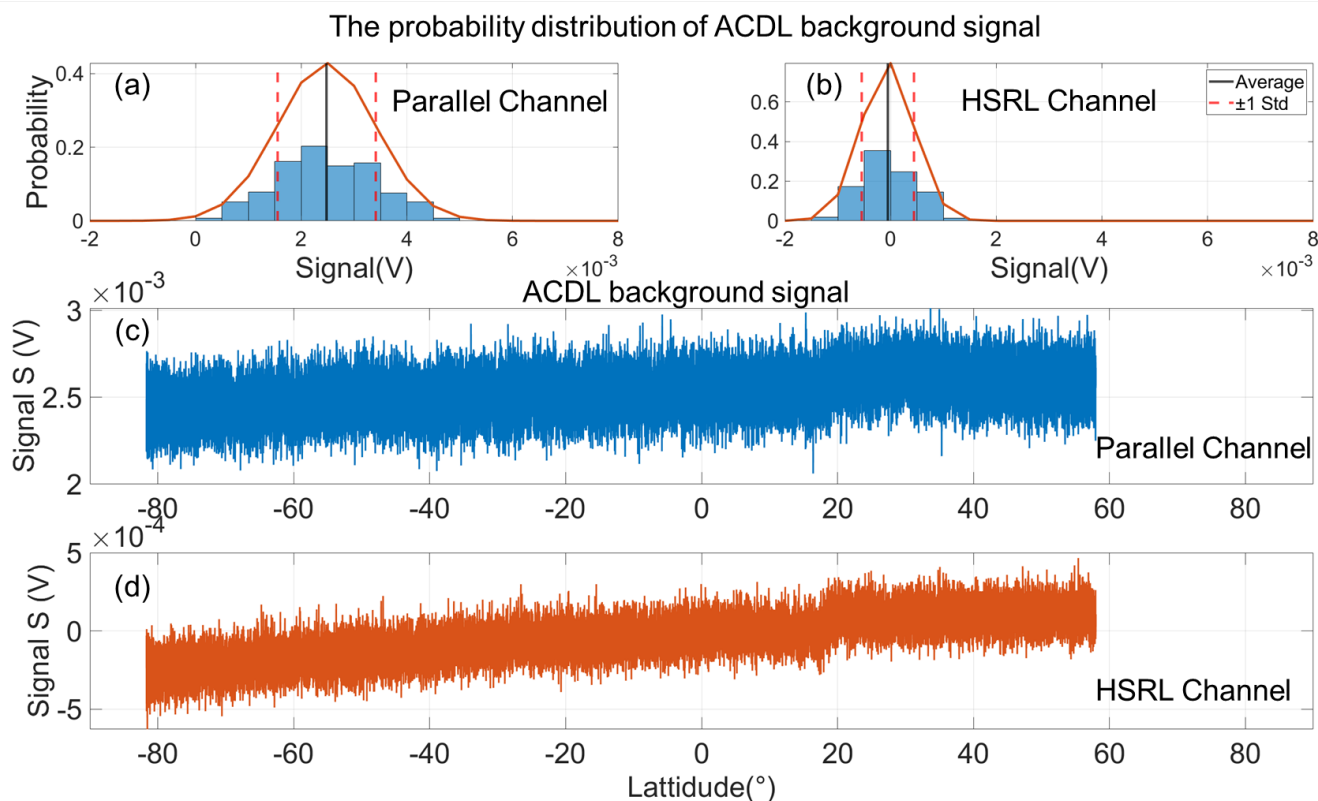
Figure 2: The ACDL collected background signal along latitude and its probability distribution in the parallel and HSRL channels (orbit 9928). (a) The probability distribution of the background signal in parallel channel and (b)HSRL channel; (c) The background signal along latitude in parallel channel and (d)HSRL channel.

The ACDL background signal acquisition employs the mean raw data from a 2km segment at the upper boundary of the data frame. As illustrated in Figure 2, the signals of the parallel and HSRL channels within the target altitude range basically obey the normal distribution, and the background signals along the latitude influenced by the solar and the dark noise, which demonstrates well stability. The synchronized article on the background signal situation and its analysis, collected by ACDL, is currently in preparation.

The calibration procedure consisting of the following steps:

Step 1: Removes the background signal from the ACDL raw signal to provide a background-free signal for subsequent calculations;

Step 2: The molecular transmittance and ozone absorption at 532 nm within the calibration regions are computed using the ERA5 atmospheric prediction model data provided by ECMWF. Additionally, the molecular backscattering at the corresponding location is calculated based on its pressure and temperature data. Then the transmittance effects due to the Fabry-Pérot etalon (F-P etalon) and the iodine vapor absorption filter following the ACDL system design are computed. Match the denoised lidar signal with the above calculated molecular and ozone transmittance, molecular backscatter coefficients and

lidar instrument transmittance in elevation and geographic coordinates. And then compute the range-scaled energy and gain-normalized signal;

Step 3: Evaluate the signal quality and atmospheric aerosol distribution, determine calibration range and horizontal average

140   distance, and screen the signals for calibration procedure;

Step 4: Calculate the calibration coefficients for the parallel and high-spectral-resolution channels, and then determine the calibration coefficients for the perpendicular-polarized channel based on the polarization gain ratio.

Step 5: Obtain the global calibration coefficients by sliding averages in the along-track and neighboring-track directions using valid data;

145   Step 6: Compute the attenuated backscatter coefficient profiles.

The flow chart for the calibration is presented in Figure 3.
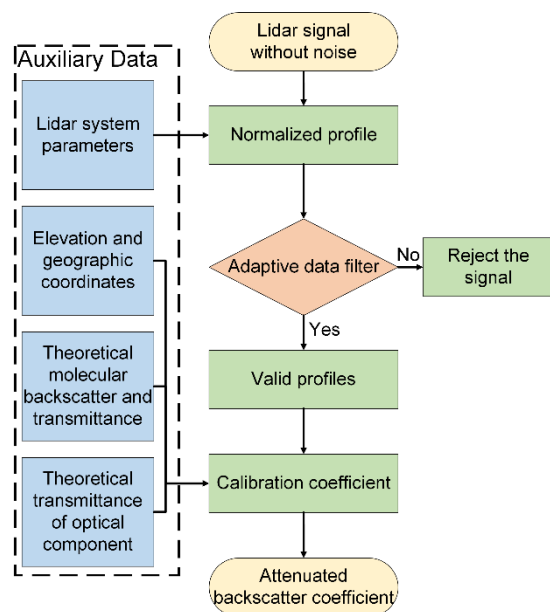
Figure 3: Flow chart of ACDL calibration. The procedure for calculating molecular and ozone transmittance, molecular backscatter coefficients, and lidar instrument transmittance in elevation and geographic coordinates are illustrated in the blue boxes; Data
150   **filtering is shaded orange; and the main calibration process are shaded green; Pre-calibration and calibrated data are shaded yellow.**

2.1 Theoretical basis and equations

The ACDL profiles are averaged vertically and horizontally on the satellite, with the averaging ratio depending on the altitude. After the geolocation and altitude corrections, the polarization and high-spectral-resolution channel data are obtained with a vertical resolution of 3 m at lower altitudes (below ~7.5 km), 24 m at higher altitudes (above ~7.5 km) along with a horizontal

155   resolution of about 0.33 km. The distance r of the scatterer from the satellite can be expressed as

$$r = \frac{z_{sat}(k_p) - z(k_p)}{\cos(\theta(k_p))},$$ (1)

where z is the height of the scatter above mean sea level, z_{sat} is the satellite altitude, k_p is the laser pulse index number, θ is the off-nadir angle.

Defining the range-scaled energy and gain-normalized signals (hereinafter normalized signal) is a necessary first step for the different channels including:

$$X^{\mathrm{P}}(z, k_p) = \frac{r^2 S^{\mathrm{P}}(z, k_p)}{E_0(k_p) G_A^P} = C^{\mathrm{P}}(k_p)\beta^{\mathrm{P}}(z, k_p)T^2(z, k_p)f_{F-P}(z, k_p) \text{ , and} \tag{2}$$

$$X^{\mathrm{M}}(z, k_p) = \frac{r^2 S^{\mathrm{M}}(z, k_p)}{E_0(k_p) G_A^M} = C^{\mathrm{M}}(k_p)\beta^{\mathrm{M}}(z, k_p)T^2(z, k_p)f_{F-P}(z, k_p)f_I(z, k_p) \text{ ,} \tag{3}$$

where X is the range-scaled signal normalized to laser energy and gain, S is the received signal, E_0 is the laser pulse energy, C is the calibration coefficient, G_A^P and G_A^M are the amplifier gains. The transmittances of F-P etalon and iodine vapor absorption filter are functions of height due to dependence on atmospheric temperature and pressure, denoted by $f_{F-P}(z)$ and $f_I(z)$. The superscript P represents the polarization channels, including both the parallel-polarized channel and the perpendicular-polarized channel. And the superscript M represents the high-spectral-resolution channel. T^2 is the two-way transmittance of the laser in the atmosphere as a function of the length of the signal optical path, and therefore is also a function of the altitude (Bodhaine et al., 1999; Collis and Russell, 1976), and is given by

$$T^2(z, k_p) = \exp\left[-2 \int_0^r \sigma(z, k_p, r')dr'\right] \text{ .} \tag{4}$$

Where σ is the volumetric extinction coefficient, given by the following equation

$$\sigma(z, k_p) = \sigma_m(z, k_p) + \sigma_{O_3}(z, k_p) + \sigma_a(z, k_p) \text{ ,} \tag{5}$$

with subscripts m, O_3, a representing, respectively, molecular scattering, ozone absorption, and aerosol scattering.

For subsequent clarification, we simplify the equations as

$$X^{\mathrm{P}} = C^{\mathrm{P}}\beta^{\mathrm{P}}T^2 f_{F-P} \text{ and} \tag{6}$$

$$X^{\mathrm{M}} = C^{\mathrm{M}}\beta^{\mathrm{M}}T^2 f_{F-P}f_I \text{ ,} \tag{7}$$

Thus, the attenuated backscattering coefficient of the polarization and the high-spectral-resolution channel (hereafter referred to as multi-channel) could be derived by applying the calibration coefficients to the corresponding normalized signals, for different channels as

$$\beta_\parallel'(z, k_p) = \frac{X^\parallel(z, k_p)}{C^\parallel(k_p)f_{F-P}} = \beta^\parallel(z, k_p)T^2(z, k_p) \text{ ,} \tag{8}$$

$$\beta_\perp'(z, k_p) = \frac{X^\perp(z, k_p)}{C^\parallel(k_p)PGR(k_p)f_{F-P}} = \beta^\perp(z, k_p)T^2(z, k_p) \text{ and} \tag{9}$$

$$\beta_M'(z, k_p) = \frac{X^{\mathrm{M}}(z, k_p)}{C^{\mathrm{M}}(k_p)f_{F-P}f_I} = \beta^{\mathrm{M}}(z, k_p)T^2(z, k_p) \text{ .} \tag{10}$$

Where the ∥ represents the parallel channel, ⊥ represents the perpendicular-polarized channel. The PGR (polarization gain ratio) is a conversion factor that quantifies the relative magnitudes of the parallel- and perpendicular-channel detector gains, detector quantum efficiencies, amplifier gains, and optical efficiencies downstream of the polarization beam splitter (Hunt et al., 2009; Alvarez et al., 2006).

2.2 Calibration procedure

The ACDL 532 nm multi-channel calibration coefficients for nighttime conditions using the molecular normalized technique. The technique requires that the backscatter in the calibration region comes primarily from molecules. To estimate the calibration coefficients, the calculated ratio is based on the normalized signal and the modelled attenuated backscatter (Russell et al., 1979; Hostetler et al., 2006; Reagan et al., 2002). The ACDL selects 31–35 km as the calibration region. The following paragraphs provide a detailed explanation of the mathematical basis for the calibration procedure.

Since there are still a small amount of aerosols present in the calibration regions (Vernier et al., 2009), the relative contribution of aerosol backscattering is evaluated by utilizing the aerosol data from SAGE III (Cisewski et al., 2014; Knepp et al., 2020). The 532 nm parallel-channel and high-spectral-resolution channel calibration coefficient equations are formed to solve for $C^{\parallel}$ and C^{M} as

$$C^{\parallel} = \frac{X^{\parallel}(z_c)}{\hat{\beta}^{\parallel}(z_c)\hat{T}^2(z_c)\hat{R}^{\parallel}(z_c)\hat{f}_{F-P}(z_c)} \text{ .and} \tag{11}$$

$$C^{M} = \frac{X^{M}(z_c)}{\hat{\beta}^{M}(z_c)\hat{T}^2(z_c)\hat{f}_{F-P}(z_c)\hat{f}_I(z_c)} \text{ .} \tag{12}$$

Where $X^{\parallel}$ and X^{M} are the normalized signal measured by ACDL, z_c is the designated altitude, and the hat notation ^ denotes the parameters estimated from an atmospheric model. The atmospheric model data include global temperature, ozone mass mixing ratio and pressure data, and are obtained from the ERA5 dataset (Hersbach et al., 2020).

The ERA5 dataset provides hourly averaged global atmospheric parameters with 37 barometric pressure levels, and on a 0.25° latitude × 0.25° longitude resolution grid. The ERA5 global data is aligned with the altitude, latitude and longitude of the ACDL profiles.

The aerosol scattering ratio in Eq. 11 is given by the following equation,

$$\hat{R}^{\parallel} = \frac{\hat{\beta}^{\parallel}(z_c)}{\hat{\beta}_m^{\parallel}(z_c)} = \frac{\hat{\beta}_m^{\parallel}(z_c) + \hat{\beta}_a^{\parallel}(z_c)}{\hat{\beta}_m^{\parallel}(z_c)}. \tag{13}$$

In Eq. (13), the total backscattering coefficient of the parallel channel is subdivided into molecular volume scattering and aerosol volume scattering, where $\hat{\beta}_m^{\parallel}(z_c)$ and $\hat{\beta}_a^{\parallel}(z_c)$ are the parallel components of the molecular and the aerosol volume backscatter coefficients (Knepp et al., 2020), respectively. The result of the aerosol scattering ratio between 31 km to 35 km calculated from the SAGE III data (2018-2022) are shown in Figure 4. To avoid additional effects introduced by using other

instruments for measurements, the calculated aerosol scatting ratio were not used in the actual calculations, only to assess the error caused by aerosol loading.
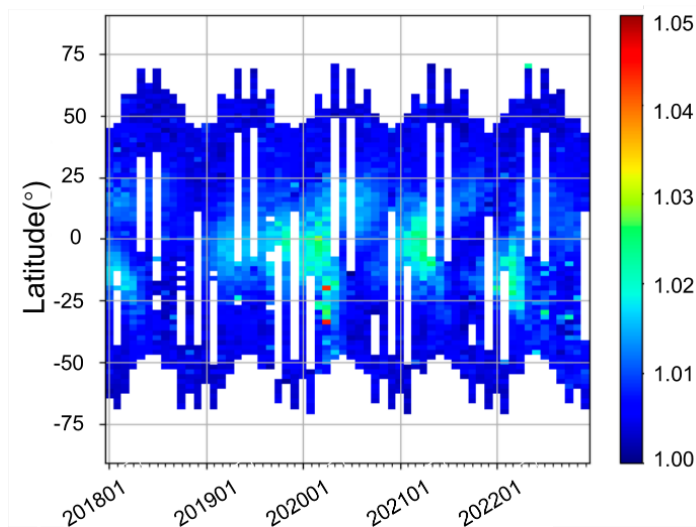
215 **Figure 4. The averaged result of the aerosol scattering ratio between 31 km to 35 km calculated from the SAGE III data (2018-2022).**

The parallel component of molecular backscatter is calculated from estimations of the total molecular backscatter $\hat{\beta}_m$ and the expected depolarization ratio for molecular backscatter δ_m.

$$\hat{\beta}^{\parallel}(z_c) = \frac{1}{1+\delta_m}\hat{\beta}_m(z_c) = 0.996\hat{\beta}_m(z_c), \tag{14}$$

with,

220 $$\delta_m = \frac{\hat{\beta}_m^{\perp}}{\hat{\beta}_m^{\parallel}} = 0.00366. \tag{15}$$

The bandwidth of the F-P narrowband filter used in the ACDL is less than 30 pm, so 0.00366 was chosen as the ratio of perpendicular to parallel backscatter as the central Cabannes line where the backscatter can be detected (She, 2001; Cairo et al., 1999).

The total molecular backscatter is obtained by calculating the product of the molecular number density and the total Rayleigh
225 scattering perpendicular section for air mass (Reagan et al., 2002; Cairo et al., 1999), by the following Eq. (16)

$$\hat{\beta}_m = \frac{\hat{\sigma}_m(z_c)}{S_m} = \frac{\hat{\sigma}_m(z_c)}{(\frac{8\pi}{3})k_{bw}}, \tag{16}$$

In Eq. 16, $S_m = (\frac{8\pi}{3})k_{bw}$ is the molecular lidar ratio (also extinction-to-backscatter ratio, Richard et al., 2001), where $k_{bw}=1.0401$ is the King factor that accounts for molecular anisotropy (Bucholtz, 1995; She, 2001; Hostetler et al., 2006). The molecular volume scattering coefficient $\hat{\sigma}_m$ can be calculated at the corresponding altitude z_c by

230 $\quad \hat{\sigma}_m(z_c) = \frac{N_A P(z_c) Q_S}{R_a T(z_c)},$ $\qquad\qquad\qquad$ (17)

At the altitude z_c, ERA5 provides the pressure $P(z_c)$ (in hPa) and the temperature $T(z_c)$ (in K) (Hersbach et al., 2020). The Avogadro's number N_A is 6.02214×10^{23} mol^{-1}, the gas constant R_a is 8.314472 J·K^{-1}mol^{-1}, and the perpendicular section for total Rayleigh scattering per molecule for 532 nm Q_S is adopted as 5.167×10^{-27} cm^2 (Hostetler et al., 2006; Bucholtz, 1995). The two-way signal attenuation $\hat{T}^2$ is defined as the attenuation of the signal from lidar transmitter to the scattering volume

235 and back to the receiver. Different from Eq. (4), the modeled attenuation for the ACDL to the calibration altitude z_c can be described with

$$\hat{T}^2(z_c) = \exp\left\{-2\int_{z_{sat}}^{z_c}[\hat{\sigma}_m(z') + \hat{\sigma}_{O_3}(z') + \hat{\sigma}_a(z')]dz'\right\}, \qquad (18)$$

The $\hat{\sigma}_{O_3}$ is given by

$$\hat{\sigma}_{O_3} = c_{O_3}\hat{\varepsilon}_{O_3}, \qquad\qquad (19)$$

240 where c_{O_3} is the Chappuis ozone absorption coefficient in m^{-1}. The ozone absorption coefficient is obtained at the correct wavelength from empirical table (Palm et al., 2012; Iqbal, 1984; Vigroux, 1953). The ε_{O_3} is the column density for ozone mass mixing ratio conversion, calculated by the following equation of

$$\hat{\varepsilon}_{O_3}(z_c) = \frac{r_{O_3}(z_c)P(z_c)}{2.14148 \times 10^{-5}RT(z_c)}. \qquad\qquad (20)$$

The ozone mass mixing ratios r_{O_3} are first converted to column density per kilometer (atmcm/km, Hersbach et al., 2020), the

245 gas constant R is 287.058 J·K^{-1}kg^{-1}. The transmittance curves calculated from the above Eq. (18) are shown in Figure 5.
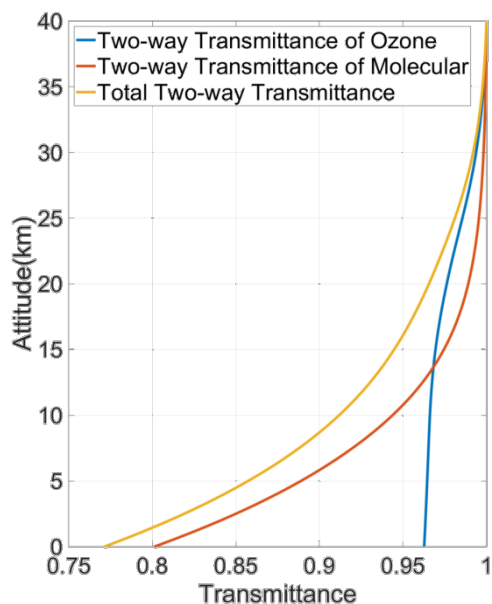
Figure 5: Two-way transmittance of ozone (blue line), molecules (orange line) and total two-way transmittance (yellow line).

Due to the variation of atmospheric molecular broadening at the calibration altitude with temperature and pressure, the transmittance of signals within both the F-P etalon and the iodine vapor absorption filter also fluctuates. The transmittance is

250   calculated under different temperature and pressure conditions. The following are the Rayleigh scattering functions of the molecular signals through the F-P etalon and the iodine vapor absorption filter (Flesia and Korb, 2000):

$$\hat{f}_{F-P}(T,P) = \int_{-\infty}^{+\infty} \mathcal{R}_m(T,P,v')\hat{F}_{F-P}(v')dv' \quad \text{and} \tag{21}$$

$$\hat{f}_I(T,P) = \int_{-\infty}^{+\infty} \mathcal{R}_m(T,P,v')\hat{F}_I(v')dv'. \tag{22}$$

Where $\mathcal{R}_m$ is the normalized Rayleigh scattering function, v is the frequency of the backscattering signal of the molecules at

255   the calibration heights, and $\hat{F}_{F-P}$, $\hat{F}_I$ are the transmittance functions of the F-P etalon and the iodine molecular absorption filter calibrated in the laboratory. The ACDL iodine molecular absorption filter uses iodine absorption line 1110 (Dong et al., 2018), with the measured transmittance spectrum as shown in Figure 6. As demonstrated in Figure 6, the molecular broadening at heights of 30-40 km extends across the absorption line 1110. Consequently, the effect of the 1110 line was rectified in the transmittance calculation. The F-P transmittance curve completely covers the scattering spectra of the molecules in the

260   calibration region, so there is no need for an additional schema in Figure 6.
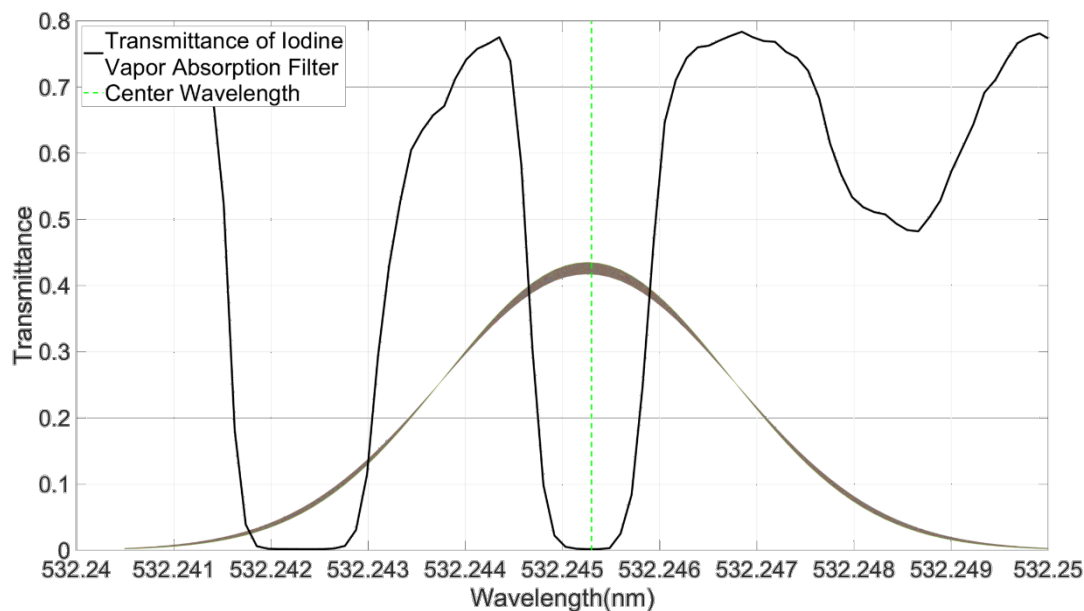
Figure 6: Transmittance function (black line) of the iodine vapor absorption filter (green dotted line means the center wavelength, and multiple color curves means normalized Rayleigh scattering function at 30–40 km).

As the principal optical path of the perpendicular-polarized channel is identical to that of the parallel-polarized channel, the

265   differentiating factor is the gain setting and beam splitter transmittance. Consequently, in the measurement, it is assumed that the operational state of the perpendicular-polarized channel is essentially equivalent to that of the parallel-polarized channel.

And the calibration of the perpendicular-polarized channel can be obtained by the relationship between the calibration coefficient of the parallel-polarized channel and the polarization gain ratio. The calibration for the perpendicular-polarized channel requires the application -of the polarization gain ratio (PGR) of the perpendicular to the parallel-polarized channel, which defined as the ratio of the two detection channel signals.

The ACDL is equipped with an insertable depolarizer to calibrate the polarization gain ratio on-board. However, based on the statistical analysis of the measured signals over a long time, it can be concluded that the gain of the ACDL is consistent with that of the ground at this stage. Concurrently, it is not necessary to activate the insertable depolarizer on board. In this study, we have employed the laboratory-calibrated gain for each channel and conducted an error analysis based on the laboratory calibration results. The polarization gain ratio is used to quantify the differences in the responsivity and gain of the two 532-nm detection channels (Powell et al., 2009; Dai et al., 2024):

$$PGR \equiv \frac{c^\perp}{c^\parallel} \approx \frac{G^\perp}{G^\parallel}, \tag{23}$$

$G^\parallel$ and $G^\perp$ are overall responsivity and gain of the parallel channel and the perpendicular channel (Hostetler et al., 2006; Powell et al., 2009). The ACDL system has undergone ground calibration, including depolarization calibration. The calibration module has been specially reserved in the spaceborne ACDL (as shown in Figure 1). In this module, a calibration beam with a known polarization state is pre-set. This, in combination with the usage of a half-wave plate, can be used for the on-orbit polarization calibrations(Alvarez et al., 2006; Powell et al., 2009; Freudenthaler, 2016).

Before commencing the calibration process, it is essential to determine the heights of the calibration region. The selection of the calibration heights for ACDL is guided by the following principles: firstly, the signal-to-noise ratio of the signal in the upper atmosphere is low, necessitating substantial data averaging; secondly, the lower atmosphere is significantly impacted by aerosols, which are unsuitable for calibration heights that should only comprise of molecular scattering (Kar et al., 2019; Kyrölä et al., 2013; Wang et al., 2020). Taking the ACDL data frame range and signal quality into account, the calibration region was set between 31 and 35 km. This altitude region in the stratosphere is sufficiently high to be relatively free of aerosols (albeit not completely so), and low enough to ensure a backscatter signal of adequate magnitude, given the mean molecular number density.

The ACDL averages the high-altitude data on the satellite and downloads the profile data with a horizontal resolution of 330 m and a vertical resolution of 24 m. However, the signal profile data quality fails to satisfy the calibration requirements, so a large amount of additional data averaging is required to obtain an accurate calibration coefficient estimate. First, we eliminate high-energy events from the signals in the calibration region, and averaged the signal horizontally into 3.6 km intervals (i.e., 11 consecutive single shot profiles). Then, these averaged data profiles are transformed into provisional calibration coefficient composite profiles by using Eqs. (24) and (25). Finally, the calibration coefficients are further averaged through a 139-point sliding average, providing the effective 500-km average between independent samples. In summary, the equation for calculating the calibration coefficients for the nighttime 532 nm parallel and high-spectral-resolution channel are as follow:

$$C(y_k) = \frac{1}{j_{31km}-j_{35km}+1}\sum_{j=j_{31km}}^{j=j_{35km}}\frac{\frac{1}{11}\sum_{i=k-5}^{i=k+5}X(z_j,y_i)}{\hat{\beta}(z_j,y_k)\hat{R}(z_j,y_k)\hat{T}^2(z_j,y_k)\hat{f}_{F-P}(z_j,y_k)}, \tag{24}$$

300 $$\tilde{C}(y_k) = \frac{1}{139}\sum_{k-69}^{k+69}C(y_k) \text{ and} \tag{25}$$

Where i and j are the index for horizontal and vertical sample in one profile, y and z are the horizontal distance and vertical distance along the track. The hat notation ~ denotes the parameters that are smoothed every 500 km along the track. Keeping the spatial resolution below 5 km could effectively remove the effect of the underlying terrain on the signal while taking into account the signal quality. Therefore, the averaging of 11 profiles is used here for computation.

305 Figure 7b and 7c illustrate the calibration coefficient C as a function of the smoothed calibration coefficient $\tilde{C}$ along latitude for the parallel channel and the high-spectral-resolution channel, respectively. An example with the orbit of 9928 on July 1st, 2022 is presented in Figure 7.

Under single-profile conditions, the correlation between the lidar received signal and the ERA5 atmospheric model increases significantly with increasing averaged vertical distance, as the choice of a longer range of calibrations helps to reduce the effect

310 of random noise. However, increasing the vertical distance is also accompanied by a significant increase in the variation of molecular backscattering coefficients. Therefore, ACDL chooses 31-35 km as the calibration region. The stratospheric aerosol content between 31 and 35 km can be non-uniform, resulting in inaccurate characterization of calibration coefficients in areas affected by aerosols and introducing additional errors. And the impact of high-energy events in certain areas (e.g. South Atlantic Anomaly, SAA, Hunt et al., 2009) can spread over a large region due to the long averaging distances.

315 To accurately calculate the global ACDL calibration coefficient, additional sliding average of 500 km in the direction of adjacent-track distances. This method requires a specific duration (usually one month) to accumulate data. During the initial data processing phase, only the 500 km along-track average is used to compute the calibration coefficients for each profile. Later, the globally averaged calibration coefficient is applied to recalibrate both the processed and unprocessed ACDL raw data during the accumulation criteria for recalibration. The horizontal resolution of ACDL is 0.33 km, and the average of 500

320 km along the orbit contains ~1500 profiles, which is basically sufficient for the computation of calibration coefficients after data filtering.
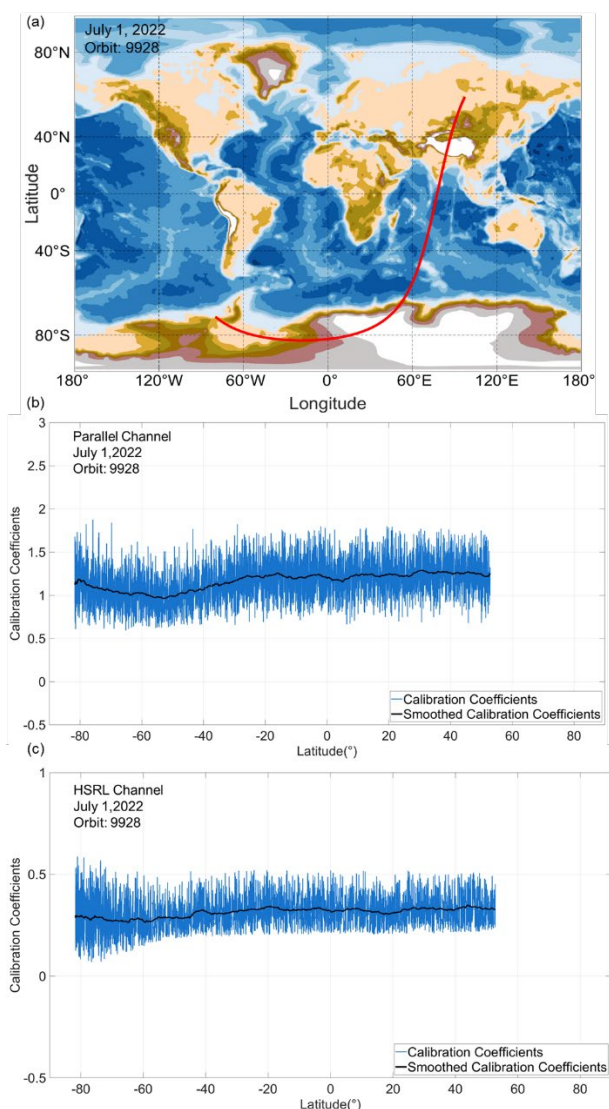
Figure 7: The calibration coefficients for each calibration region, the calibration coefficients for parallel-polarized channel normalized by 2.11*10[8] m³srJ⁻¹, and 5.21*10[8] m³srJ⁻¹ for the HSRL channel. (a) The example orbit 9928 for July 1ˢᵗ, 2022; (b) The estimated parallel channel calibration coefficients from the 3.6 km average (blue line) and the smoothed calibration coefficient results after 500 km sliding average (black line) are displayed. (c) The estimated high-spectral-resolution channel calibration coefficients from the 3.6 km average (blue lines) and the smoothed calibration coefficient results after 500 km sliding average (black line) are presented. The orbital track segment that corresponds to calibration coefficients can be found in the upper right corner of the figure.

2.3 Adaptive data filter

The lidar data contains random signal spikes, which can significantly impact the calibration coefficients (Lee et al., 2008; Kar et al., 2018). These high-energy events are mainly concentrated in the SAA region, but also occur randomly throughout the detection (Hunt et al., 2009). Although the PMTs mounted on the ACDL are of shielded design, it is also necessary to filter

the collected data to exclude spikes from the data used for calibration. The calibration procedure for ACDL involves a filtering

335 technique that consists of three sequential steps to filter the signal extracted in the previous step.

Step 1: Each signal in the calibration area (altitude range of 31-35 km and horizontal range of 3.6 km) is first filtered using upper and lower limits based on the theoretical values X, as well as the fluctuation of the measured profiles. The Eq. (26) are used to determine the thresholds of X_T for the parallel channel and the high-spectral-resolution channel, respectively.

$$X_T = \hat{X}(l) \pm k_m \Delta \text{X}, \tag{26}$$

340 Where $\hat{X}(l)$ is the theoretical value of $\text{X}(z_k)$ at position l, which corresponding to the latitude of the signal profile. The subscript T denotes the threshold range of the filter. The scaling factors k_m are defined empirically, vary across channels and can be adjusted. The selection of the scaling factor is based on the statistical analysis of the signal intensity distribution of the high-energy signals. Since the ACDL signal basically follows the Poisson distribution, with drastic changes in the low value region and smoothness in the high value region, different factors are selected in the high and low value regions to ensure the

345 accuracy of the data.

Theoretical profiles are estimated from the modelled molecular number density within the calibration region. The random uncertainties ΔX quantify the random errors (shot noises) in the signals. The equations below define the ΔX as a function of latitude,

$$\delta(z_{j,k}) = X(z_{j,k}) - \hat{X}(z_{j,k}) \tag{27}$$

350 $$\Delta X = \sqrt{\frac{\sum_1^n (\delta(z_{j,k}) - \bar{\delta})^2}{n}}. \tag{28}$$

Where $z_{j,k}$ is the location of the calibration profile, n is the number of the averaged bins, δ is the difference between measured and theoretical values, the $\bar{\delta}$ is mean of the δ, ΔX represents the standard deviation of the δ.

Step 2: The second step of the filtering technique involves the use of the Noise-to-Signal Ratio (NSR, Lee et al., 2008; Powell et al., 2009) test to evaluate signals in the pre-calibration area between 31–35 km vertically and 3.6 km horizontally. This test

355 determines whether there are significant variations in signal magnitude within the specified region. Use the data filtered in the first step as valid data X_{valid} for the subsequent NSR calculation:

$$NSR = \frac{\sigma_{std}(X_{valid})}{\mu(X_{valid})}. \tag{29}$$

Where σ_{std} is the standard deviation and μ is the mean value of the valid signals X. The resulting values are compared to an empirically defined NSR. Any high-energy events exceeding the NSR threshold get excluded from the calibration procedure.

360 Signals that are valid within the calibration range that has been accepted are then entered into the next step of the calibration process.
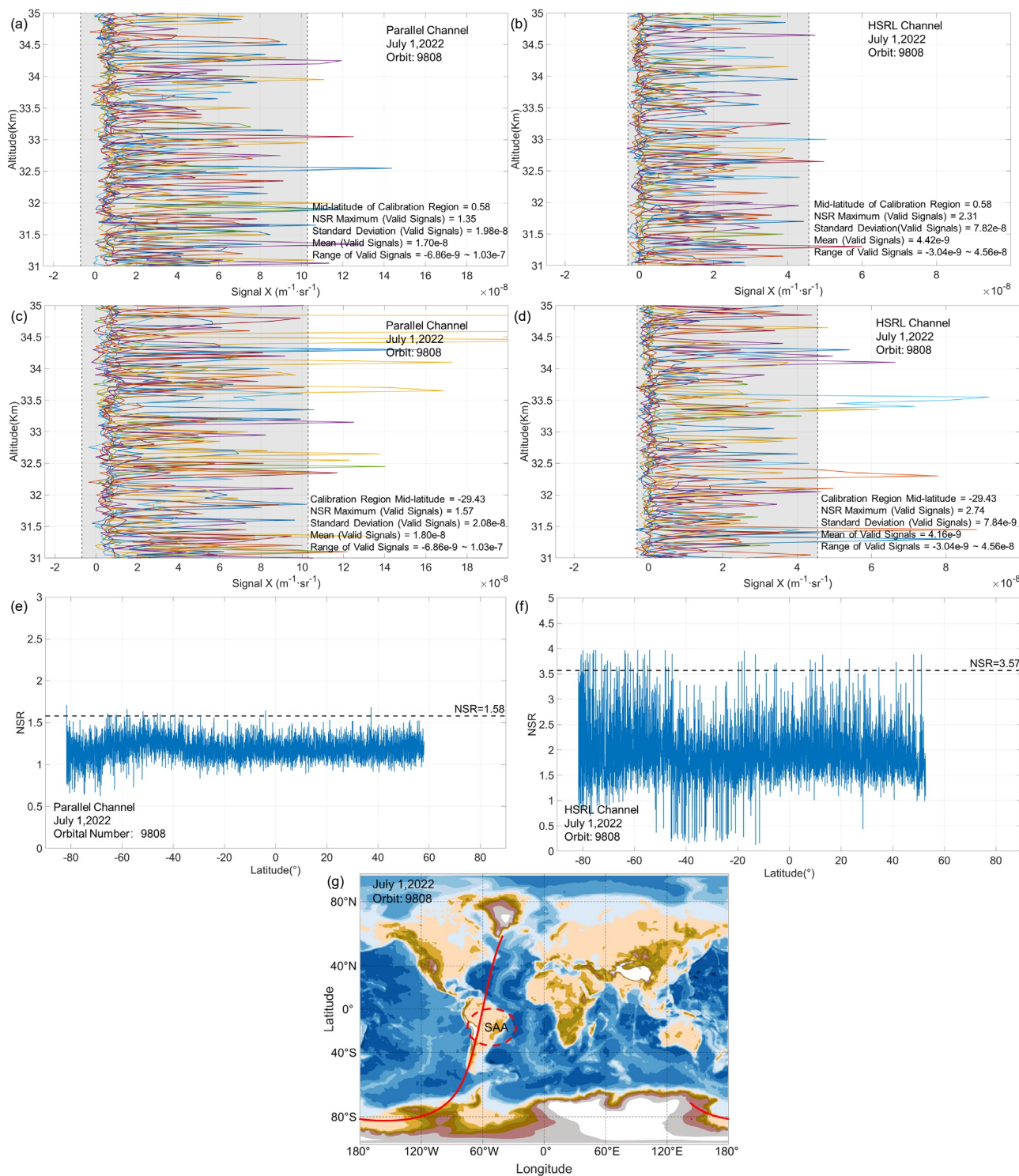
Figure 8: Schematic representation of the signal filtering by NSR. The 11 $X^{\parallel}$ signal profiles of the parallel channel located near the (a) edge and (c) centre of SAA; The 11 X^{M} signal profiles of the high-spectral-resolution channel located near the (b) edge and (d) centre of SAA; (e) The parallel channel NSR as a function of the corresponding latitude (orbit 9808), the dotted line indicates the NSR threshold value of 1.58; (f) The high-spectral-resolution channel NSR as a function of the corresponding latitude (orbit 9808), the dotted line indicates the NSR threshold value of 3.57; (g) An example orbit passing through the SAA region, orbit 9808. The valid signals detected by the filter, as indicated by the shaded areas. The colored lines in the figure indicate 11 consecutive observation profiles.

The NSR values as a function of latitude in the parallel and high-spectral-resolution channels are illustrated in Figure 8 for the same orbit (as seen in Figure 8g). Due to the differences in optical path, optical sensitivity and transmittance of optical elements between the ACDL polarization channel and HSRL channel, resulting in different levels of random error and signal averages for the two channels, so the different NSR thresholds are selected.

Additionally, Figure 8e and 8f demonstrate the application of the NSR test within calibration regions. Figure 8a to 8d display comparisons of signals and high-energy events between the centre and edge profiles of the SAA. The adaptive filter identifies valid signals within the shaded regions, and excludes the data that falls outside of the shaded range. The remaining profiles were utilized as valid data in the subsequent stage of the averaging calculation.
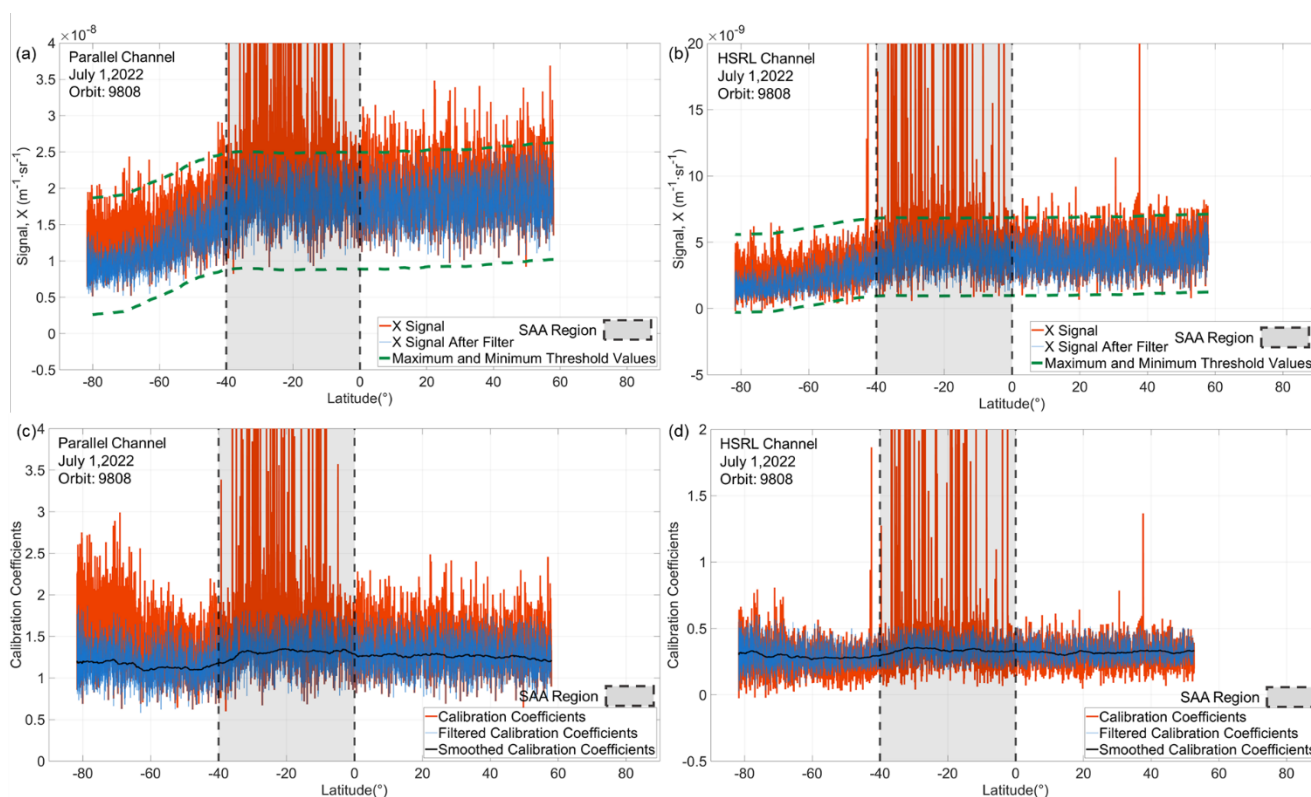
Figure 9: Schematic of the original signal and calibration coefficients after filtering (orbit 9808), the calibration coefficients for parallel-polarized channel normalized by $2.11*10^{8}$ $m^{3}srJ^{-1}$, and $5.21*10^{8}$ $m^{3}srJ^{-1}$ for the HSRL channel. (a) The average signal $X^{\parallel}$ as a function of the corresponding latitude for altitudes between 31 and 35 km, 1 July 2022. Within the SAA, there is a significant variation in the original signal, as indicated by the red lines. The adaptive filter defines the minimum and maximum values with dotted lines, and the blue lines show the signals after filter. And the green dotted lines indicate the range of thresholds; (b) The

average signal X^M as a function of the corresponding latitude for altitudes between 31 and 35 km, orbit 9808. The lines in Figure 9b
385 **have the same meaning as in Figure 9a; (c) The filtered (blue) and unfiltered (orange lines) calibration coefficients of the parallel**
channel. The black line plots the smoothed calibration coefficients; (d) The filtered (blue) and unfiltered (orange lines) calibration
coefficients of the high-spectral-resolution channel. The black line plots the smoothed calibration coefficients.

Step 3: In the third step, the population of candidate profiles is being filtered prior to computing the mean using threshold
determined by Eqs. (26) - (28) above. The final filter evaluates whether the mean values of the signal profiles available for the
390 calibration calculation fall within the pre-set threshold range.

Figure 9a and 9b exemplify the application of the adaptive filter, depicting the $X^\parallel$ and X^M signals as a function of latitude
before and after the screening. The data pertains to the 9808 orbit 31–35 km altitude average on July 1st, 2022. As depicted in
the graph, the signal demonstrates significant fluctuations while passing through the SAA region, which spans from the equator
to about 40°S. High-energy events in the calibration regions create remarkably high signal spikes, but the ACDL measured
395 signal results in less pronounced negative signal spikes. Figure 9c and 9d depict the screened profiles, displaying the calibration
coefficients before and after the data filtering. The results indicate that the adaptive filter effectively removes the errors caused
by high-energy events when calculating the calibration coefficients, allowing the ACDL calibration procedure to accurately
determine 532 nm calibration coefficients.

The filtering causes some profiles to be rejected, resulting in missing calibration coefficients in some regions. In these cases,
400 the nearest valid calibration coefficients (guaranteed closest in distance) are selected as replacements. The percentage of
rejected profiles for ACDL nightime calibration as shown in Figure 10.
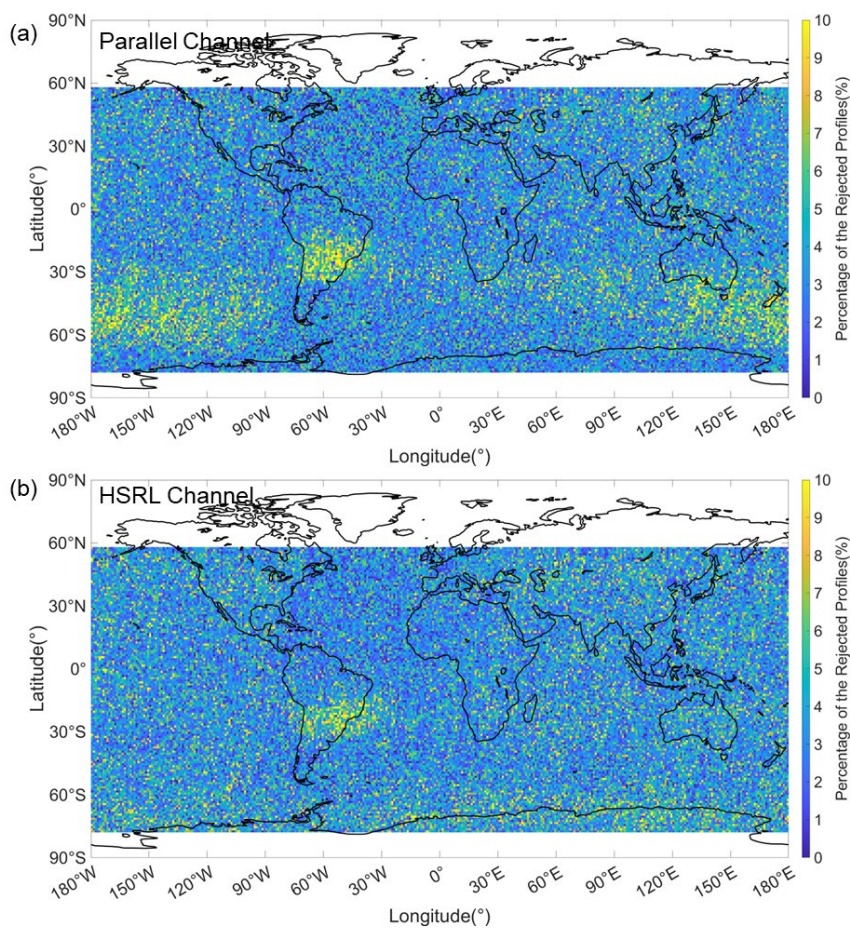
Figure 10: The percentage of rejected profiles for ACDL nighttime calibration (July). (a) Parallel-polarized channel, and (b) HSRL channel

3. Assessment

Assessments are continuously conducted on the ACDL nighttime 532 nm multi-channel calibration procedure during the mission. The assessment is evaluated through error analysis and validation. The error analysis assesses systematic and random errors, and validation is achieved by utilizing attenuated backscatter coefficients and clear-sky attenuated scattering ratios. Validation tests, such as comparing airborne lidar observations and ground-based lidar networks, will be carried out in the further research.

3.1 Error analysis

The uncertainty of the calibration coefficients comprises systematic and random errors, which can be expressed as,

$$\left(\frac{\Delta C}{C}\right)^2 = \left(\frac{\Delta C}{C}\right)^2_{System} + \left(\frac{\Delta C}{C}\right)^2_{Random}. \tag{30}$$

The systematic uncertainty component of the parallel channel (Powell et al., 2009) is given by

$$\left(\frac{\Delta C^{\parallel}}{C^{\parallel}}\right)^2_{System} \approx \left[\frac{\Delta \hat{R}^{\parallel}(z_c)}{\hat{R}^{\parallel}(z_c)}\right]^2 + \left[\frac{\Delta \hat{\beta}_m^{\parallel}(z_c)}{\hat{\beta}_m^{\parallel}(z_c)}\right]^2 + \left[\frac{\Delta \hat{T}^{\parallel}(z_c)}{\hat{T}^{\parallel}(z_c)}\right]^2 + \left[\frac{\Delta \hat{T}_{F-P}(z_c)}{\hat{T}_{F-P}(z_c)}\right]^2 + \left[\frac{\Delta \hat{E}(z_c)}{\hat{E}(z_c)}\right]^2. \tag{31}$$

Table 2 presents the estimates of the systematic error components for the ACDL nighttime 532 nm calibration procedure. The source of uncertainty analysis should reasonably apply to calibration regions between 31 and 35 km in the stratosphere. As more accurate information is acquired on the precision of the products used for calculations, estimations of the error terms contributing will be revised. Currently, these diverse components create a comprehensive relative systematic error of ~5% for $\Delta C^{\parallel}/C^{\parallel}$. The error resulting from the two-way transmittance T^2 is negligible, at less than 0.005%, and is disregarded in the calculations conducted.

Table 2: Systematic error components for the 532 nm parallel channel calibration coefficient.

$\left(\frac{\Delta C^{\parallel}}{C^{\parallel}}\right)_S$	$\frac{\Delta R^{\parallel}(z_c)}{R^{\parallel}}$	$\frac{\Delta \hat{\beta}_m^{\parallel}(z_c)}{\hat{\beta}_m^{\parallel}(z_c)}$	$\frac{\Delta \hat{T}_{F-P}(z_c)}{\hat{T}_{F-P}(z_c)}$	$\frac{\Delta \hat{E}(z_c)}{\hat{E}(z_c)}$
0.045	0.03	0.03 (Hersbach et al., 2020)	0.01	0.01

The systematic uncertainty component of high-spectral-resolution channel is given by

$$\left(\frac{\Delta C^M}{C^M}\right)^2_{System} \approx \left[\frac{\Delta \hat{\beta}_m^M(z_c)}{\hat{\beta}_m^M(z_c)}\right]^2 + \left[\frac{\Delta \hat{T}^M(z_c)}{\hat{T}^M(z_c)}\right]^2 + \left[\frac{\Delta \hat{T}_{F-P}(z_c)}{\hat{T}_{F-P}(z_c)}\right]^2 + \left[\frac{\Delta \hat{T}_I(z_c)}{\hat{T}_I(z_c)}\right]^2 + \left[\frac{\Delta \hat{E}(z_c)}{\hat{E}(z_c)}\right]^2, \tag{32}$$

The error evaluation of the high-spectral-resolution channel follows the same method, with Table 3 listing the current best estimations of the systematic error components. Presently, the equation above can be used to calculate the overall relative systematic error $\Delta C^M/C^M$ is ~4%.

Table 3: Systematic error components for the 532 nm high-spectral-resolution channel calibration coefficient.

$\left(\frac{\Delta C^M}{C^M}\right)_S$	$\frac{\Delta \hat{\beta}_m^M(z_c)}{\hat{\beta}_m^M(z_c)}$	$\frac{\Delta \hat{T}_{F-P}(z_c)}{\hat{T}_{F-P}(z_c)}$	$\frac{\Delta \hat{T}_I(z_c)}{\hat{T}_I(z_c)}$	$\frac{\Delta \hat{E}(z_c)}{\hat{E}(z_c)}$
0.035	0.03 (Hersbach et al., 2020)	0.01	0.01	0.01

The error analysis of the ACDL nighttime calibration procedure refer to the CALIPSO mission, which is also a spaceborne lidar system for cloud and aerosol measurements.

The CALIPSO Version 3 calibration developed a theoretical systematic uncertainty estimate of ~5% for the nighttime parallel channel calibration coefficient (Powell et al., 2009). Subsequently, collocated airborne HSRL measurements were used to produce an Version 3 empirical systematic uncertainty estimate of 3.6% ± 2.2% (Rogers et al., 2011). By moving the CALIPSO calibration region up to 36-39 km (Kar et al., 2018), the CALIPSO project reduced this empirical uncertainty estimate to 1.6% ± 2.4% in their Version 4 data release. The theoretically derived systematic error estimate for ACDL nighttime 532 nm parallel channel is commensurate with the theoretically derived estimate for CALIPSO Version 3 calibration (Powell et al., 2009), but higher than empirically established calibration bias of the CALIPSO Version 4 data release (Kar et al., 2018).

The averaged random uncertainty, $\Delta C(y_k)$, is given by

$$\Delta C = \sqrt{\frac{\Sigma_1^n (C(z_{j,k}) - \hat{C}(z_{j,k}))^2}{n}}. \tag{33}$$

440   The random uncertainty is estimated by calculating the Standard deviation of the calibration coefficients. In the estimation process of the random uncertainty, only the error attributable to the calculated calibration coefficients itself is considered. More influences of the error attributable to the calibration coefficients are further considered in the subsequent evaluation process. The uncertainty in calibration coefficient for the perpendicular-polarized channel can be calculated by considering the error in parallel channel and the error in polarization gain ratio, as shown in the following equation (Powell et al., 2009):

445   $$\left(\frac{\Delta C^\perp}{C^\perp}\right)^2 = \left(\frac{\Delta C^\parallel}{C^\parallel}\right)^2 + \left(\frac{\Delta PGR}{PGR}\right)^2. \tag{34}$$

The currently used ground-calibrated PGR has a measurement error of ~1%, and the estimation includes both random and systematic errors, taking into account crosstalk between channels.

3.2 Validation

The molecular normalization technique relies on matching the signal in the purely molecular atmospheric region at high altitude,
450   to achieve calibration coefficients applicable throughout the full vertical extent of the individual profiles. To accurately assess the calibration coefficients, the matching of the attenuated backscatter coefficients in the calibration region with the model must be determined first. Figure 11 presents the results of 31-35 km calibrated averaged signals.
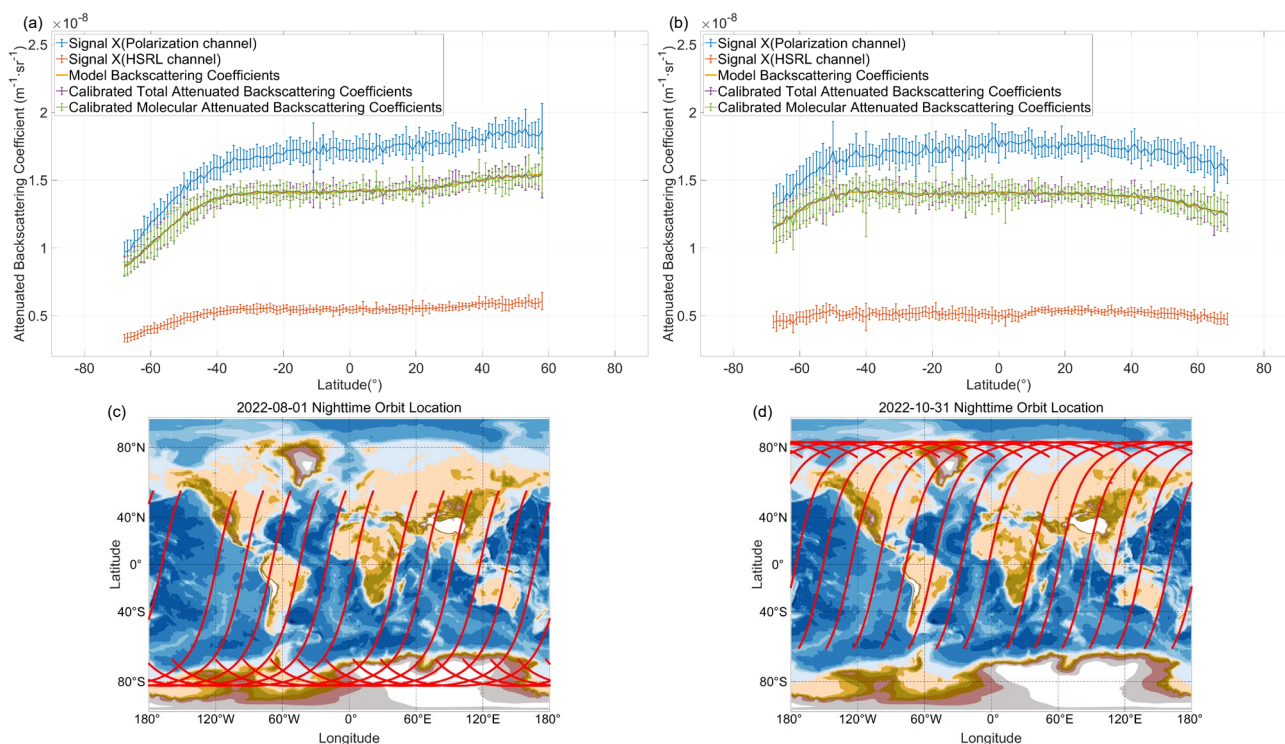
Figure 11: Average for the measured total polarization and HSRL signal (m-1sr-1, blue and orange line), model estimates (m^{-1}sr^{-1}, yellow line), and calibrated total polarization and HSRL signal (m-1sr-1, purple and green line) along the latitude. (a) and (b): These values on August 1st and October 31st; (c) and (d): The orbits of DQ-1 nighttime measurement for August 1st and October 31st, 2022. The estimated average values were calculated over a vertical distance of 31–35 km and a horizontal sliding average of 1°.

After the calibration procedure, the signal X was corrected to align with the modeled attenuation backscatter coefficient, as demonstrated in Figure 11 on August 1st and October 31st, 2022. The results indicate that the calibrated backscatter coefficients have a total relative error of less than 2% comparing with the mean value of the modeled results, achieve a satisfactory match within the range of 31–35 km. The relative error is calculated using the following formula:

$$\Delta\beta'(z_{31-35},\ l) = \frac{\beta'(z_{31-35},l) - \widehat{\beta'}(z_{31-35},l)}{\beta'(z_{31-35},l)} \times 100\%, \tag{35}$$

where β' is the mean of calibrated attenuated backscatter coefficient measured at latitude l and altitudes of 31–35 km, $\widehat{\beta'}$ is the theoretically attenuated backscatter coefficient derived from model data, and $\Delta\beta'$ is the relative error.

To assessed the performance of the calibration procedure, the clear-air scattering ratios were calculated by using attenuated backscatter data from the ACDL polarization channel and the HSRL channel. These values are then compared to the theoretical clear-air scattering ratio of 1. Regions with extremely low aerosol loading are referred as clear-air region. Previous studies have demonstrated that aerosol loading at altitudes between 8 km and 12 km is typically quite low, leading to frequent observations of total scattering ratio observed to be close to 1 (Powell et al., 2009 & 2010). The 8-12 km is quite a low altitude, and it is difficult to ensure that the assumption that the 12-40 km range contains no aerosols is valid even under clear-air conditions. However, since the ACDL has both a polarization channel and a HSRL channel, the attenuated total backscattering coefficient and the attenuated molecular backscattering coefficient can be obtained simultaneously. The clear-air scattering ratios R_{CA} is defined as

$$R_{CA}(z_{8-12}, k) = \frac{\beta'_{total}(z_{8-12},k)}{\beta'_{m}(z_{8-12},k)}. \tag{36}$$

where k is the index of profile and z_{8-12} denotes the altitude range used to calculate the scattering ratio, β'_{total} and β'_{m} is the total and molecular calibrated attenuated backscatter coefficient measured by ACDL (polarization and HSRL channel, separately) at the zrange, and k is the index of profile used to calculate the scattering ratio. Thus, even at low altitudes, the unattenuated aerosol scattering ratios can be obtained directly because both measurement channels have the same attenuation characteristics (as shown in Eq. (37)). Therefore, ACDL adopts 8–12 km as a clear-air region to calculate the scattering ratio to validate the multi-channel calibration algorithm. Through this comparison, it is possible to identify the existing bias in the ACDL calibration. The measured attenuated backscatter coefficients are determined by molecular backscatter, faint aerosol backscatter, and extinction within the atmosphere (McGill et al., 2007). Expanding Eq. (36) yields

$$\begin{aligned} R_{CA}(z_{8-12}, k) &= \frac{[\beta_m(z_{8-12},k) + \beta_a(z_{8-12},k)]T_m^2(z_{8-12},k)T_{O_3}^2(z_{8-12},k)T_a^2(z_{8-12},k)}{\beta_m(z_{8-12},k)\widehat{T}_m^2(z_{8-12},k)\widehat{T}_{O_3}^2(z_{8-12},k)T_a^2(z_{8-12},k)} \\ &= \frac{\beta_m(z_{8-12},k) + \beta_a(z_{8-12},k)}{\beta_m(z_{8-12},k)} \\ &= 1 + \frac{\beta_a(z_{8-12},k)}{\beta_m(z_{8-12},k)} \end{aligned} . \tag{37}$$

At low aerosol contents, the difference between the clear-air scattering ratios calculated from the calibrated attenuated total

485   backscatter coefficients and the molecular backscatter estimate is less than the systematic error (~5% for polarization channel and ~3.5% for HSRL channel; ~6.1% for clear-air scattering ratio), which is the relative calibration uncertainty. After completing the signal calibration, the difference between the calculated clear-air scattering ratio and the estimated molecular backscatter is within 6.1% uncertainty at the 8–12 km region (as illustrated in Figure 12). To reduce the effect of noise, the profile of the clear-air scattering ratio R_{CA200} was averaged over ~200 km [12] segment by using Eq. (38) (as illustrated in

490   Figure 12)

$$R_{CA200} = \frac{1}{60} \sum_{k=1}^{60} \langle R_{CA}(z_{8-12}, k) \rangle. \tag{38}$$
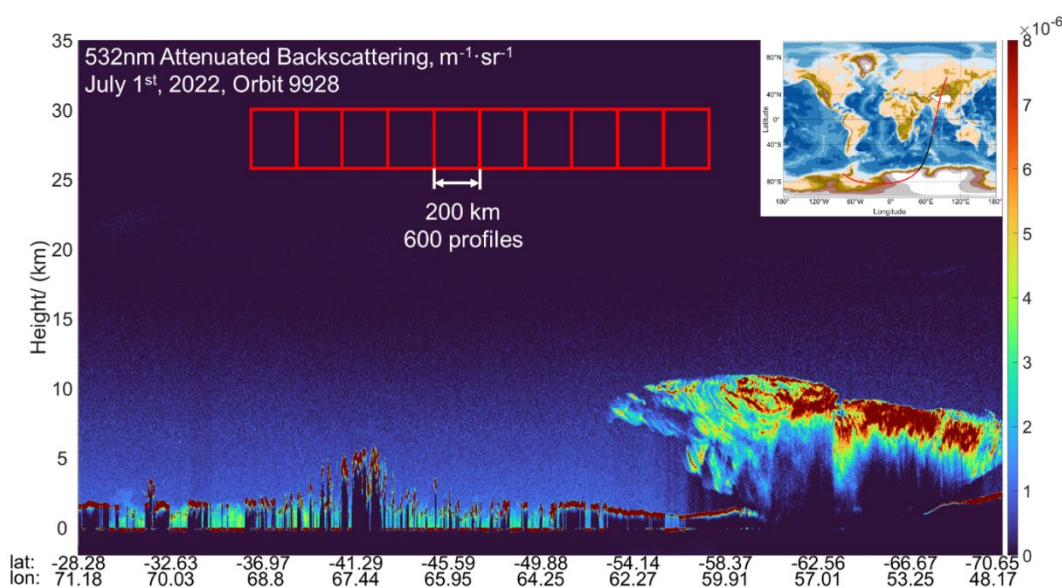
Figure 12: Lidar 532 nm total attenuated backscatter coefficient (m⁻¹sr⁻¹, 1 July 2022). The clear-sky regions are illustrated by red boxes, spanning 200 km in length and ranging from 26 to 30 km in altitude. The upper right figure displays the range of track (black

495   **line).**

Figure 13 (a) illustrates four consecutive profiles of the clear-air scattering ratio $R_{CA}(z_{8-12}, k)$ for polarization and HSRL channels from July 1st, 2022. The profiles display the ratio fluctuations and are at single profile resolution. A composite profile was produced by averaging ten profiles (3.3-km horizontal resolution) over the altitude range. And the horizontal distance between profiles is approximately 4 km. The dashed line is present in each plot to represents the scattering ratio of 1.0 for

500   reference. The average scattering ratio for profiles is represented by the vertical solid lines. In these cases, the average scattering ratios deviate partially from the expected 1±0.06 due to the shot noise of the single and the impact of the faint aerosol.
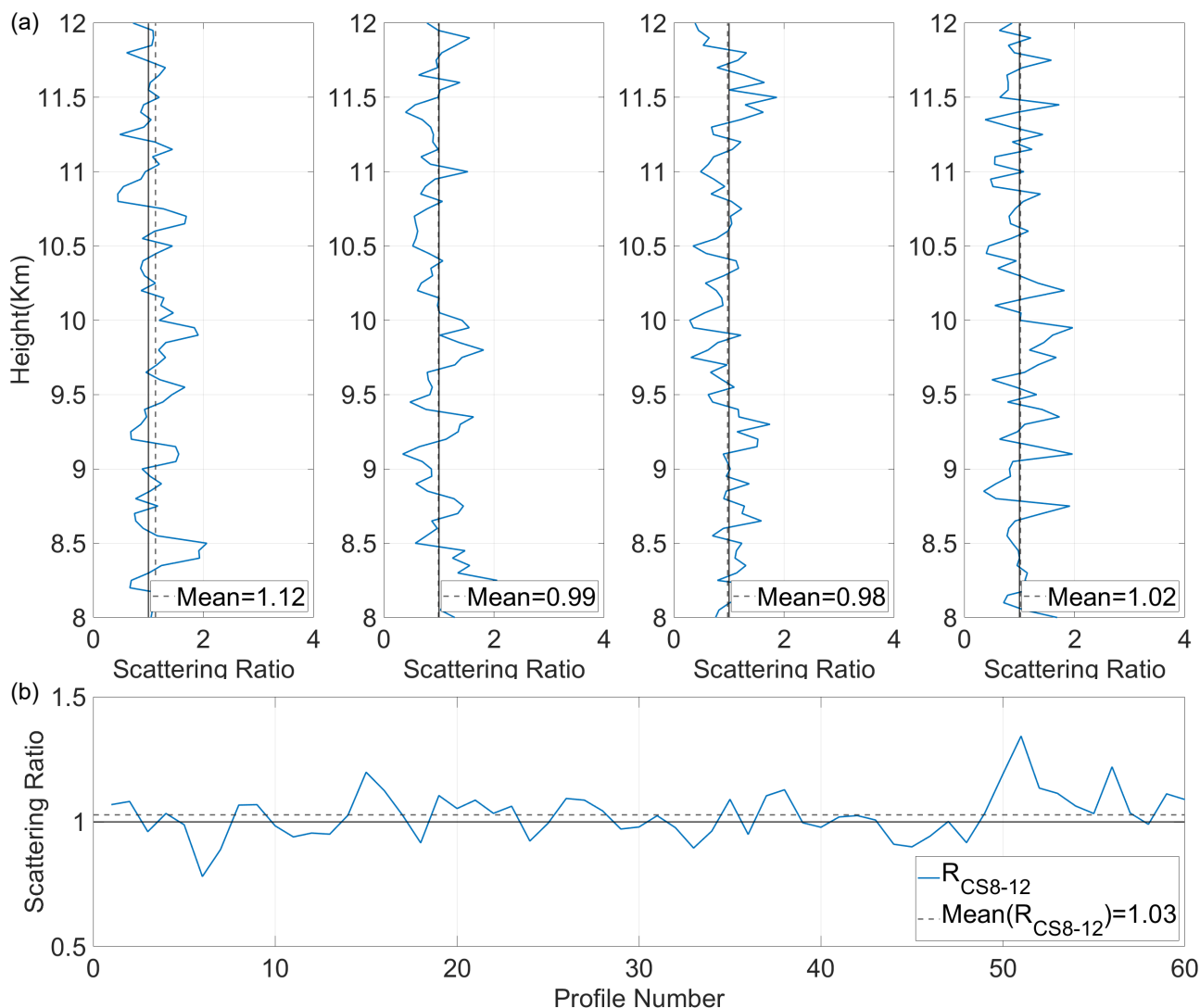
Figure 13: The averaged clear-air scattering ratio from July 1st, 2022. (a) Four consecutive clear-air scattering ratio profiles (3.3-km horizontal resolution, 8–12 km); (b) The mean of the averaged clear-air scattering ratio for 60-profiles (~200 km segment, blue line). The mean of averaged clear-air scattering ratio (black solid line), and the expected value of 1.0 (black dotted line).

505

Figure 13(b) displays the mean computed over 60-profiles (~200 km, Powell et al., 2009) for clear-air scattering ratio R_{CA200} at a 3.3-km horizontal resolution, the 60-profile mean is about 1.03. Although the mean ratio for single profile was not all as expected, the average over 200 km kept the mean attenuation scattering ratio results within the range of 1±0.06. The Standard deviation as shown in Figure 13 depicting that the fluctuations primarily stem from the shot noise.

510 The above two validation methods verify that the ACDL calibration procedure performs well at both high and low altitudes. While the underflight experiments synchronized with the on-board ACDL have not yet been implemented, steady progress is

being made. As a supplement, the validation of ACDL profiles have conducted a profile comparison utilizing a dual-wavelength polarization Raman lidar and the CALIPSO satellite. The Total Attenuation Backscatter Coefficient (TABC) and the Volume Depolarization Ratio (VDR) have been validated, respectively (Liu et al., 2024). The validation results further
515   demonstrate the accuracy of the calibration algorithm.

4. Discussion and outlook

The molecular normalization calibration technique applied to ACDL has been successfully applied to its polarization channel, and demonstrates its feasibility for high-spectral-resolution channel. Planned algorithm improvements include updating the adaptive filter and further removing the effects of dark noise.
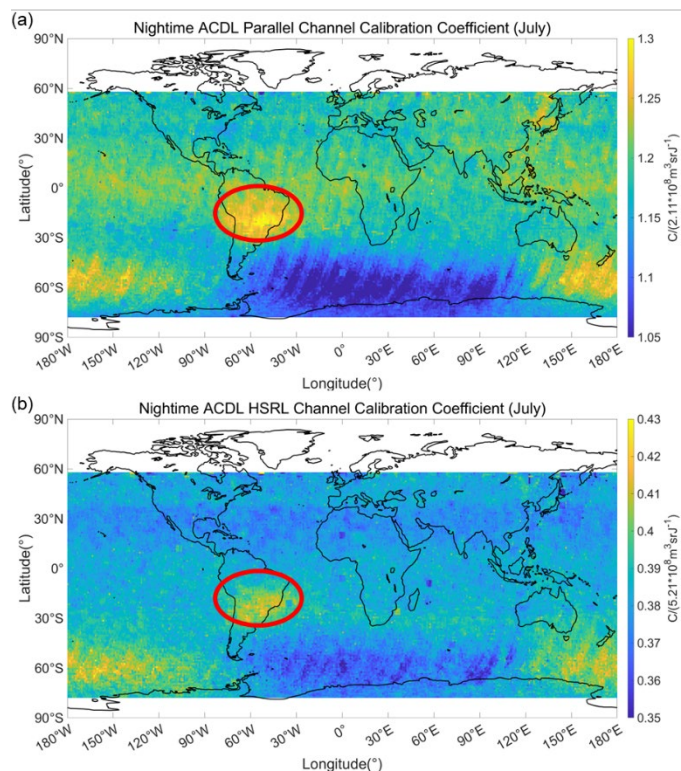
Figure 14: Result of global calibration coefficient on a 1° latitude × 1° longitude grid for July, 2022. (a) The results of parallel channel and (b) the results of high-spectral-resolution channel. The red circles indicate the SAA region.

Figure 14 illustrates the result of global calibration coefficient on a 1° latitude × 1° longitude grid for July, 2022. The Arctic and adjacent regions are in the polar day range in July, so there are no calibration coefficients for nighttime. The calibration
525   procedures use denoised lidar signals and filters have reduced the effects of high-energy events, but strong signals due to random noise can still lead to the fluctuate of calibration. During nighttime measurements, the SAA region produced higher calibration coefficients than expected, which is due to the high-energy incident was not filtered completely. In addition,

elliptical regions of increased calibration coefficients near the poles can be seen, due to auroras near the poles [28]. The influence of these events also spreads as the sliding average frame progresses. Evaluation of the impacts of different dark noise feature for lidar signals at night and rectifying the calibration coefficients in such regions will be conducted in the follow-up study.

In the future, the ACDL scientific team plans to continuously conduct validation tests to verify the reliability of the calibration algorithm. This will involve adding simultaneous observations using various types of lidar and extending the range of validation. In the future development of the enhanced instrument, the scientific team will fully consider the issues of dark noise and random high-energy events. The instrument proposed improvements include increasing the reception of dark noise signals and reducing background noise level.

5. Summary

This paper presents a comprehensive calibration procedure for the first spaceborne high-spectral-resolution lidar with an iodine vapor absorption filter, ACDL on board DQ-1. The calibration procedure is established on the denoised raw data and combines the transmittance of scattered signals matched to elevation and geographic coordinates, to calculate the range-scaled, gain and energy normalized signal. Valid profiles are extracted for calibration by using adaptive filters, thus obtaining the calibration coefficients for each profile. The calibration coefficients obtained by applying a 500-km sliding average, are used as the final results for calculating the global attenuated backscatter coefficient profiles. The calibration coefficients for the perpendicular-polarized channel relative to the parallel-polarized channel are determined through the utilization of the PGR.

This study analyzed the error sources of the multi-channel calibration coefficients and validated the results. The mean value of the attenuated backscatter coefficients in the calibration region shows a relative error of less than ~1%. The clear-air scattering ratios demonstrate that the ACDL polarization channel calibration is reliable and operates within the expected error range of approximately 6%. The effective application of the ACDL nighttime calibration algorithm will enhance the calibration of the daytime orbit and other channels, thereby improving the quality of subsequent data products.

As the core component of the entire ACDL calibration procedure, the scientific team is committed to improving the daytime 532 nm calibration algorithm and the 1064 nm calibration algorithm. However, the calibration process has yet to account for the impact of background noise and high calibration coefficients in specific regions. In future research, the scientific team plans to improve the nighttime 532 nm multi-channel calibration algorithm and introduce additional validation tools.

Data availability

Data underlying the results presented in this paper are not publicly available at this time but may be obtained from the authors upon reasonable request. The ERA5 dataset are downloaded via the website: https://cds.climate.copernicus.eu/cdsapp#!/

dataset/reanalysis-era5-pressure-levels?tab=form (last access: 11 October 2023). The SAGE III dataset are downloaded via the website: https://asdc.larc.nasa.gov/project/SAGE%20III-ISS(last access: 11 October 2023).

Author contributions

560   F. Meng, J. Tang and G. Dai conceived and designed the Nighttime multi-Channel Calibration Algorithms; F. Meng and G. Dai wrote the manuscript; W. Long, X. Song, K. Sun and J. Liu participated in the algorithm development and data analysis; J. Tang, S. Wu and W. Chen provided the supervision and participated in the scientific discussion. All the co-authors reviewed and edited the manuscript.

Competing interests

565   The authors declare that they have no conflict of interest.

Acknowledgments

This study has been jointly supported by the National Key Research and Development Program of China (2023YFC3007801), the National Natural Science Foundation of China (NSFC) under grant U2106210, the Laoshan Laboratory Science and Technology Innovation Projects under grant LSKJ202201202, National Key Research and Development Program of China

570   (2022YFB3901705), Qingdao Future Industry Cultivation Special Emerging Industry Plan 22-3-4-xxgg-8-gx, International Partnership Program of Chinese Academy of Sciences (18123KYSB20210013), and Shanghai Science and Technology Innovation Action Plan (22dz208700).

References

Alverez, J.M., Vaughan, M.A., Hostetler, C.A., Hunt, W.H., and Winker, D.M.: Calibration Technique for Polarization–

575   Sensitive Lidars, J Atmos Ocean Tech, 23(5), 683–699, doi: 10.1175/jtech1872.1, 2006.

Bodhaine, B.A., Wood, N.B., Dutton, E.G., and Al., E.: On Rayleigh Optical Depth Calculations, J Atmos Ocean Tech, 16(11), 1854–1861, doi: 10.1175/1520–0426(1999)016<1854:ORODC>2.0.CO;2, 1999.

Bucholtz, A.: Rayleigh–scattering calculations for the terrestrial atmosphere, Appl Optics, 34(15), 2765–2773, 10.1364/AO.34.002765, doi: 10.1364/AO.34.002765, 1995.

580   Cairo, F., Di Donfrancesco, G., Adriani, A., Pulvirenti, L., and Fierli, F.: Comparison of various linear depolarization parameters measured by lidar, Appl Optics, 21, 4425–4432, doi: 10.1364/AO.38.004425, 1999.

Chen, W., Liu, J., Hou, X., Zang, H., Ma, X., Wan, Y., and Zhu, X.: Lidar Technology for Atmosphere Environment Monitoring Satellite, Aerospace Shanghai (in Chinese and English), 3, 13–20, 110, doi: 10.19328/j.cnki.2096-8655.2023.03.002, 2023.

585 Cisewski, M., Zawodny, J., Gasbarre, J., Eckman, R., Topiwala, N., Rodriguez-Alvarez, O., Cheek, D., Hall, S., Meynart, R., Neeck, S.P., and Shimoda, H.: The Stratospheric Aerosol and Gas Experiment (SAGE III) on the International Space Station (ISS) Mission: Proc. of SPIE Vol. 9241, pp 924107-1- 7 SPIE, doi:10.1117/12.2073131,2014.

Collis, R.T.H., and Russell, P.B.: Lidar Measurement of Particles and Gases,in:Laser Monitoring of the Atmosphere, edited by: Hinkley, E.D., Chapter 4, doi: 10.1007/3–540–07743–X_18, 1976.

590 Dai, G., Wu, S., Long, W., Liu, J., Xie, Y., Sun, K., Meng, F., Song, X., Huang, Z., and Chen, W.: Aerosol and cloud data processing and optical property retrieval algorithms for the spaceborne ACDL/DQ-1, Atmos. Meas. Tech., 17, 1879–1890, https://doi.org/10.5194/amt-17-1879-2024, 2024.

Dong, J., Liu, J., Bi, D., Ma, X., Zhu, X., and Chen, W.: Optimal iodine absorption line applied for spaceborne high spectral resolution lidar, Appl Optics, 5413-5419, doi: 10.1364/AO.57.005413, 2018.

595 Flesia, C., and Korb, C.L.: Theory of the double–edge molecular technique for Doppler lidar wind measurement, Appl Optics, 38(3), 432–440, doi: 10.1364/AO.38.000432, 1999.

Freudenthaler, V.: About the effects of polarising optics on lidar signals and the Δ90-calibration, Atmos Meas Tech, 9, 4181-4255, 10.5194/amt-9-4181-2016, 2016.

Getzewich, B.J., Vaughan, M.A., Hunt, W.H., Avery, M.A., Powell, K.A., Tackett, J.L., Winker, D.M., Kar, J., Lee, K., and 600 Toth, T.D.: CALIPSO lidar calibration at 532 nm: version 4 daytime algorithm, Atmos Meas Tech, 11, 6309–6326, doi: 10.5194/amt–11–6309–2018, 2018.

Hersbach, H., Bell, B., Berrisford, P., Hirahara, S., Horányi, A., Muñoz Sabater, J., Nicolas, J., Peubey, C., Radu, R., Schepers, D., Simmons, A., Soci, C., Abdalla, S., Abellan, X., Balsamo, G., Bechtold, P., Biavati, G., Bidlot, J., Bonavita, M., De Chiara, G., Dahlgren, P., Dee, D., Diamantakis, M., Dragani, R., Flemming, J., Forbes, R., Fuentes, M., Geer, A., Haimberger, L., 605 Healy, S., Hogan, R.J., Hólm, E., Janisková, M., Keeley, S., Laloyaux, P., Lopez, P., Lupu, C., Radnoti, G., de Rosnay, P., Rozum, I., Vamborg, F., Villaume, S., and Thépaut, J.N.: The ERA5 global reanalysis, Q J Roy Meteor Soc, 146, 1999–2049, doi: 10.1002/qj.3803, 2020.

Hostetler, C. A., Liu, Z., Reagan, J., Vaughan, M., Winker, D., Osborn, M., Hunt, W. H., Powell, K. A., and Trepte, C.: CALIOP Algorithm Theoretical Basis Document, Calibration and Level 1 Data Products, PC–SCI–201, NASA Langley 610 Research Center, Hampton, VA 23681, 66 pp., available at: http://www–calipso.larc.nasa.gov/resources/project_documentatio n.php (last access: 12 October 2023), 2006.

Hunt, W.H., Winker, D.M., Vaughan, M.A., Powell, K.A., Lucker, P.L., and Weimer, C.: CALIPSO Lidar Description and Performance Assessment, J Atmos Ocean Tech, 26, 1214–1228, doi: 10.1175/2009JTECHA1223.1, 2009.

Iqbal M.: An introduction to solar radiation, in: Solar Radiation, edited by: Page, V., Chapter 10, pp295–301., doi: 615 10.1016/B978–0–12–373750–2.50009–4, 1983.

Kar, J., Lee, K., Vaughan, M.A., Tackett, J.L., Trepte, C.R., Winker, D.M., Lucker, P.L., and Getzewich, B.J.: CALIPSO level 3 stratospheric aerosol profile product: version 1.00 algorithm description and initial assessment, Atmos Meas Tech, 12, 6173–6191, doi: 10.5194/amt-12-6173-2019, 2019.

Kar, J., Vaughan, M.A., Lee, K.P., Tackett, J.L., Avery, M.A., Garnier, A., Getzewich, B.J., Hunt, W.H., Josset, D., Liu, Z.,
620   Lucker, P.L., Magill, B., Omar, A.H., Pelon, J., Rogers, R.R., Toth, T.D., Trepte, C.R., Vernier, J.P., Winker, D.M., and Young, S.A.: CALIPSO Lidar Calibration at 532 nm: Version 4 Nighttime Algorithm, Atmos Meas Tech, 11, 1459–1479, doi: 10.5194/amt–11–1459–2018, 2018.

Knepp, T. N., Thomason, L., Roell, M., Damadeo, R., Leavor, K., Leblanc, T., Chouza, F., Khaykin, S., Godin-Beekmann, S., and Flittner, D.: Evaluation of a method for converting Stratospheric Aerosol and Gas Experiment (SAGE) extinction
625   coefficients to backscatter coefficients for intercomparison with lidar observations, Atmos. Meas. Tech., 13, 4261–4276, https://doi.org/10.5194/amt-13-4261-2020, 2020.

Kyrölä, E., Laine, M., Sofieva, V., Tamminen, J., Päivärinta, S.M., Tukiainen, S., Zawodny, J., and Thomason, L.: Combined SAGE II–GOMOS ozone profile data set for 1984–2011 and trend analysis of the vertical distribution of ozone, Atmos Chem Phys, 13, 10645–10658, doi: 10.5194/acp–13–10645–2013, 2013.

630   Lee, K.P., Vaughan, M.A., Liu, Z.Y., Hunt, W.H., and Powell, K.A.: Revised Calibration Strategy for The CALIOP 532 nm Channel: Part I – Nighttime: Proc. 24th Int. Laser Radar Conf., Boulder, CO, International Coordination–group for Laser Atmospheric Studies, pp 1173–1176, available at: https://ntrs.nasa.gov/api/citations/20080023850/downloads/20080023850.pdf (last access: 12 October 2023), 2008.

Liu, D., Zheng, Z., Chen, W., Wang, Z., Li, W., Ke, J., Zhang, Y., Chen, S., Cheng, C., and Wang, S.: Performance estimation
635   of space–borne high–spectral–resolution lidar for cloud and aerosol optical properties at 532 nm, Opt Express, 27, A481–A494, doi: 10.1364/OE.27.00A481, 2019.

Liu, Q., Huang, Z., Liu, J., Chen, W., Dong, Q., Wu, S., Dai, G., Li, M., Li, W., Li, Z., Song, X., and Xie, Y.: Validation of initial observation from the first spaceborne high-spectral-resolution lidar with a ground-based lidar network, Atmos. Meas. Tech., 17, 1403–1417, https://doi.org/10.5194/amt-17-1403-2024, 2024.

640   McGill, M.J., Vaughan, M.A., Trepte, C.R., Hart, W.D., Hlavka, D.L., Winker, D.M., and Kuehn, R.: Airborne validation of spatial properties measured by the CALIPSO lidar, Journal of Geophysical Research: Atmospheres, 112, doi: 10.1029/2007JD008768, 2007.

Osborn, M.T.: Calibration of LITE Data: NASA CONFERENCE PUBLICATION, pp 245–248 NASA, 1998.

Palm, S. P., Hart, W. D., Hlavka, D. L., Welton, E. J., and Spinhirne, J.D.: The Algorithm Theoretical Basis Document for the
645   GLAS Atmospheric Data Products, NASA/TM–2012–208641/Vol 6, NASA Goddard Space Flight Center, Greenbelt, MD 20771, 148pp., available at: https://ntrs.nasa.gov/api/citations/20120016956/downloads/20120016956.pdf (last access: 12 October 2023), 2012.

Palm, S. P., Yang, Y., Herzfeld, U., and Hancock., D.: Ice, Cloud, and Land Elevation Satellite (ICESat–2) Project Algorithm Theoretical Basis Document for the Atmosphere, Part I: Level 2 and 3 Data Products, Version 6, NASA Goddard Space Flight

650   Center, Greenbelt, MD 20771, 119pp., available at: https://icesat–2.gsfc.nasa.gov/sites/default/files/page_files/ICESat2_ ATL04_ATL09_ATBD_PartI_r006.pdf (last access: 12 October 2023), 2022.

Pauly, R. M., Yorks, J. E., Hlavka, D. L., McGill, M. J., Amiridis, V., Palm, S. P., Rodier, S. D., Vaughan, M. A., Selmer, P. A., Kupchock, A. W., Baars, H., and Gialitaki, A.: Cloud-Aerosol Transport System (CATS) 1064 nm calibration and validation, Atmos. Meas. Tech., 12, 6241–6258, https://doi.org/10.5194/amt-12-6241-2019, 2019.

655   Pierre, H. F., Vincent, L., Pauline, M., Thomas, Fl., Juan, C., Alain, D., Mathieu, O., and Dorit, H.: ADM–Aeolus L2A Algorithm Theoretical Baseline Document, AE–TN–IPSL–GS–001, Version 5.7, European Space Agency, Daumesnil, Paris 75012, 92pp., available at: https://earth.esa.int/eogateway/documents/20142/37627/Aeolus–L2A–Algorithm–Theoretical– Baseline–Document.pdf/73aac3e2–8812–565c–e787–9a31011d5b06?version=1.0&t=1631019544898   (last   access: 12 October 2023), 2020

660   Powell, K.A., Hostetler, C.A., Vaughan, M.A., Lee, K., Trepte, C.R., Rogers, R.R., Winker, D.M., Liu, Z., Kuehn, R.E., Hunt, W.H., and Young, S.A.: CALIPSO Lidar Calibration Algorithms. Part I: Nighttime 532–nm Parallel Channel and 532–nm Perpendicular Channel, J Atmos Ocean Tech, 26, 2015–2033, doi: 10.1175/2009JTECHA1242.1, 2009.

Powell, K.A., Vaughan, M.A., Rogers, R.R., Kuehn, R.E., Hunt, W.H., Lee, K.P., and Murray, T.D.: The CALIOP 532–nm channel daytime calibration: Version 3 algorithm: Proceedings of the 25th International Laser Radar Conference, pp 1367–

665   1370, doi: 10.1175/2009JTECHA1242.1, 2010.

Reagan, J.A., Wang, X., and Osborn, M.T.: Spaceborne lidar calibration from cirrus and molecular backscatter returns, Ieee T Geosci Remote, 40, 2285–2290, doi: 10.1109/TGRS.2002.802464, 2002.

Richard B Miles, Walter R Lempert, and Joseph N Forkey: Laser Rayleigh scattering, Meas. Sci. Technol., 12, R33, 10.1088/0957-0233/12/5/201, 2001.

670   Russell, P.B., Swissler, T.J., and McCormick, M.P.: Methodology for error analysis and simulation of lidar aerosol measurements, Appl Optics, 18(22), 3783–3797, 10.1364/AO.18.003783, 1979.

She, C.Y.: Spectral structure of laser light scattering revisited: bandwidths of nonresonant scattering lidars, Appl Optics, 40, 4875–4884, doi: 10.1364/ao.40.004875, 2001.

Vaughan, M., Garnier, A., Josset, D., Avery, M., Lee, K., Liu, Z., Hunt, W., Pelon, J., Hu, Y., Burton, S., Hair, J., Tackett,

675   J.L., Getzewich, B., Kar, J., and Rodier, S.: CALIPSO lidar calibration at 1064 nm: version 4 algorithm, Atmos Meas Tech, 12, 51–82, doi: 10.5194/amt–12–51–2019, 2019.

Vaughan, M.A., Liu, Z., McGill, M.J., Hu, Y., and Obland, M.D.: On the spectral dependence of backscatter from cirrus clouds: Assessing CALIOP's 1064 nm calibration assumptions using cloud physics lidar measurements, Journal of Geophysical Research: Atmospheres, 115, doi: 10.1029/2009JD013086, 2010.

680   Vaughan, M.A., Powell, K.A., Winker, D.M., Hostetler, C.A., Kuehn, R.E., Hunt, W.H., Getzewich, B.J., Young, S.A., Liu, Z., and McGill, M.J.: Fully Automated Detection of Cloud and Aerosol Layers in the CALIPSO Lidar Measurements, J Atmos Ocean Tech, 26, 2034–2050, doi: 10.1175/2009JTECHA1228.1, 2009.

Vaughan, M.A., Young, S.A., Winker, D.M., Powell, K.A., Omar, A.H., Liu, Z., Hu, Y., and Hostetler, C.A.: Fully automated analysis of space–based lidar data: an overview of the CALIPSO retrieval algorithms and data products, pp 16–30 SPIE, doi: 685   10.1117/12.572024, 2004.

Vernier, J.P., Pommereau, J.P., Garnier, A., Pelon, J., Larsen, N., Nielsen, J., Christensen, T., Cairo, F., Thomason, L.W., Leblanc, T., and McDermid, I.S.: Tropical stratospheric aerosol layer from CALIPSO lidar observations, Journal of Geophysical Research: Atmospheres, 114, doi: 10.1029/2009JD011946, 2009.

Vigroux, E.: Contribution à l'étude expérimentale de l'absorption de l'ozone, in:Annales de physique. EDP Sciences, 12(8), 690   pp709–762., doi: 10.1051/anphys/195312080709, 1953.

Wang, H.J.R., Damadeo, R., Flittner, D., Kramarova, N., Taha, G., Davis, S., Thompson, A.M., Strahan, S., Wang, Y., Froidevaux, L., Degenstein, D., Bourassa, A., Steinbrecht, W., Walker, K.A., Querel, R., Leblanc, T., Godin Beekmann, S., Hurst, D., and Hall, E.: Validation of SAGE III/ISS Solar Occultation Ozone Products With Correlative Satellite and Ground-Based Measurements, Journal of Geophysical Research. Atmospheres, 125, 10.1029/2020JD032430, 2020.

695   Wang, S., Ke, J., Chen, S., Zheng, Z., Cheng, C., Tong, B., Liu, J., Liu, D., and Chen, W.: Performance Evaluation of Spaceborne Integrated Path Differential Absorption Lidar for Carbon Dioxide Detection at 1572 nm, Remote Sens–Basel, 12, 2570, doi: 10.3390/rs12162570, 2020.

Wehr, T., Kubota, T., Tzeremes, G., Wallace, K., Nakatsuka, H., Ohno, Y., Koopman, R., Rusli, S., Kikuchi, M., Eisinger, M., Tanaka, T., Taga, M., Deghaye, P., Tomita, E., and Bernaerts, D.: The EarthCARE mission – science and system overview, 700   Atmos Meas Tech, 16, 3581–3608, doi: 10.5194/amt–16–3581–2023, 2023.

Yorks, J. E., Palm, S. P., Hlavka, D. L., McGill, M. J., Nowottnick, E., Selmer, P., and Hart, W. D.: The Cloud-Aerosol Transport System (CATS) algorithm theoretical basis document, available at: http://cats.gsfc.nasa.gov/media/docs/CATS_ATBD.pdf (last access: 12 October 2023), 2015.

Zhu, W., Lv, L. Q., Wei, Z. K., Cao, Q., Dong, C. Z., and Wang, F. Y.: Design and Technological Characteristics for DQ–1 705   Satellite System, Aerospace Shanghai (in Chinese and English), 40, 1–12, doi: 10.19328/j.cnki.2096–8655.2023.03.001, 2023.